International Journal of Solids and Structures 48 (2011) 3194–3208

Contents lists available at ScienceDirect

International Journal of Solids and Structures

journal homepage: www.elsevier.com/locate/ijsolstr

A fast volume integral equation method for elastic wave propagation in a half space

Terumi Touhei *

Department of Civil Engineering, Tokyo University of Science, 2641 Yamazaki, Noda 278-8510, Japan

ARTICLE INFO

Article history:
Received 28 January 2011
Received in revised form 11 July 2011
Available online 29 July 2011

Keywords:
Volume integral equation
Fast method
Elastic half space
Scattering problem
Generalized Fourier transform
Krylov subspace iteration technique
MPI parallel processing

ABSTRACT

A fast method for solving the volume integral equation is developed for scattering analysis of elastic wave propagation in a half space. The proposed method applies the fast generalized Fourier transform and inverse transform formulated in the present study to the Krylov subspace method. The amount of calculations required for the proposed method is $O(N\log N)$, where N is the number of grid points used to model the elastic half space. Furthermore, the MPI parallel algorithm for the generalized Fourier transform is presented for further reduction of the CPU time. Numerical calculations are performed in order to examine the effects of the number of sampling grid points as well as their intervals on the solutions of the volume integral equation and the CPU time required for the analysis. In addition, comparisons of the proposed method with the previous method based on the trapezoidal approach (Touhei, 2009) are also performed in order to discuss the properties of the solution of the present method.

1. Introduction

The application of integral equation methods to engineering problems has become widespread. Since the 1980s, there have been a number of analyses of scattered waves by means of integral equation methods. For example, Colton and Kress (1998) reported a survey of a vast number of articles on forward and inverse scattering analyses. They reported methods for acoustic and electromagnetic wave propagation based on the theory of operators (Colton and Kress, 1983, 1998). Guzina et al. (2003) considered the problem of mapping underground cavities from surface seismic measurements based on a regularized boundary integral equation. The present author introduced a complete eigenfunction expansion form of the Green's function for an elastic layered half space that is applicable to the boundary integral equation method (Touhei, 2003). Manolis et al. (2004) considered elastic wave scattering due to cracks in inhomogeneous geological continua by introducing the boundary integral equation. Not only boundary integral equation methods, but also a type of volume integral equation known as the Lippmann–Schwinger equation (Ikebe, 1960) has been applied to elastic or electromagnetic scattering problems. For example, Hudson and Heritage (1981) applied the Born approximation of the solution of the volume integral equation to seismic scattering problems. Yang et al. (2008) proposed a conjugate gradient fast Fourier transform (CG-FFT) approach to solve elastic scattering problems. De Zaeytijd et al. (2008) proposed the fast Fourier transform and the high-frequency multilevel fast multipole algorithm (MLFMA-FFT) for analyzing electromagnetic waves.

The present author has previously presented a volume integral equation method based on the wavenumber domain formulation for an elastic scattering problem (Touhei, 2009 and Touhei et al., 2009). The previous method uses the Fourier transform to construct the Krylov subspace according to the mathematical form of the volume integral equation in the wavenumber domain. As a result, it was not necessary to calculate a coefficient matrix for the volume integral equation. Furthermore, the development of a fast method for an elastic full space by means of the ordinary fast Fourier transform was simple (Touhei et al., 2009). On the other hand, a fast method for an elastic half space has not yet been established (Touhei, 2009) because the kernel of the generalized Fourier transform that is required in order to formulate a fast algorithm is very complicated.

Under these circumstances, the motivation for the present study is to establish a fast method for solving the volume integral equation for an elastic half space. The essential consideration of the proposed formulation is to decompose the complicated kernel of the generalized Fourier transform into the ordinary Fourier transform and the Laplace transform to which the fast algorithm can be applied. In the following, the discussion begins with the theoretical formulation, in which the role of the generalized Fourier transform and the kernel of the generalized Fourier transform are clarified. Then, a fast algorithm for the generalized Fourier transform is presented. The amount of computation for the proposed method is $O(N\log N)$, where N is the number of grid points used

* Tel.: +81 4 7122 9629; fax: +81 4 7123 9766.
E-mail address: touhei@rs.noda.tus.ac.jp

0020-7683/$ - see front matter © 2011 Elsevier Ltd. All rights reserved.
doi:10.1016/j.ijsolstr.2011.07.013

for modeling the elastic half space. Based on the fast algorithm, a method for message-passing interface (MPI) parallel computation (Pacheco, 1997) is also presented. Several numerical examples are presented in order to examine the effects of the number of sampling grid points and their intervals on numerical solutions as well as the CPU time required for the calculations. Verification of the amount of computation $O(N\log N)$ is also carried out based on the numerical results. Comparisons of the present solutions with solutions obtained by the previous method based on the trapezoidal approach (Touhei, 2009) are performed in order to investigate the properties of the present method.

2. Theoretical formulation

2.1. Volume integral equation for a scattering problem

Fig. 1 shows the concept of the problem defined in the present article. A point source is applied to a 3-D elastic half space. Scattered waves are generated by the interaction between the waves from the point source and the presence of the fluctuations. A Cartesian coordinate system is used to describe the wave field, in which the spatial point is expressed as:

$$x = (x_1, x_2, x_3) \in \mathbb{R}^2 \times \mathbb{R}_+ = \mathbb{R}^3_+, \tag{1}$$

where the subscript index indicates the component of the Cartesian coordinate system. In the following, the summation convention is applied to the subscript indices describing the Cartesian coordinate system. The free boundary of the half space is denoted by $x_3 = 0$. The fluctuation of the wave field is expressed by the Lamé constants and the mass density such that:

$$\begin{aligned} \lambda(x) &= \lambda_0 + \tilde{\lambda}(x), \\ \mu(x) &= \mu_0 + \tilde{\mu}(x), \\ \rho(x) &= \rho_0 + \tilde{\rho}(x), \end{aligned} \tag{2}$$

where λ_0, μ_0, and ρ_0 are the background Lamé constants and the mass density, and $\tilde{\lambda}$, $\tilde{\mu}$, and $\tilde{\rho}$, respectively, are their fluctuations. The P and S wave velocities for the background structure are denoted by c_L and c_T, which are obtained from:

$$c_L = \sqrt{(\lambda_0 + 2\mu_0)/\rho_0}, \quad c_T = \sqrt{\mu_0/\rho_0}. \tag{3}$$

Let the time factor of the wave field be $\exp(i\omega t)$, where ω is the circular frequency and t is the time. The governing equations, as well as the boundary conditions for the present problem, are given as:

$$\begin{aligned} \left(L_{ij}(\partial_1, \partial_2, \partial_3) + \delta_{ij}\rho_0\omega^2\right)u_j(x) &= N_{ij}(\partial_1, \partial_2, \partial_3, x)u_j(x) \\ &\quad - q_i\delta\left(x - x_{(s)}\right), \end{aligned} \tag{4}$$

$$P_{ij}(\partial_1, \partial_2, \partial_3, x)u_j(x) = 0, \quad (\text{at } x_3 = 0), \tag{5}$$

where u_i is the total displacement field, δ_{ij} is the Kronecker delta, $\delta(\cdot)$ is the Dirac delta function, $x_{(s)}$ is the spatial point to which the point force is applied, q_i is the amplitude of the point source, and L_{ij}, N_{ij}, and P_{ij} are the differential operators constructed by the background structure of the wave field and their fluctuations, respectively. The explicit forms of the operators L_{ij}, N_{ij}, and P_{ij} are expressed as:

$$L_{ij}(\partial_1, \partial_2, \partial_3) = (\lambda_0 + \mu_0)\partial_i\partial_j + \mu_0\delta_{ij}\partial_k\partial_k, \tag{6}$$

$$\begin{aligned} N_{ij}(\partial_1, \partial_2, \partial_3, x) = &-\left(\tilde{\lambda}(x) + \tilde{\mu}(x)\right)\partial_i\partial_j - \delta_{ij}\tilde{\mu}(x)\partial_k\partial_k - \partial_i\tilde{\lambda}(x)\partial_j \\ &- \delta_{ij}\partial_k\tilde{\mu}(x)\partial_k - \partial_j\tilde{\mu}(x)\partial_i - \delta_{ij}\tilde{\rho}(x)\omega^2, \end{aligned} \tag{7}$$

$$\left[P_{ij}(\partial_1, \partial_2, \partial_3, x)\right] = \begin{bmatrix} \mu(x)\partial_3 & 0 & \mu(x)\partial_1 \\ 0 & \mu(x)\partial_3 & \mu(x)\partial_2 \\ \lambda(x)\partial_1 & \lambda(x)\partial_2 & (\lambda(x) + 2\mu(x))\partial_3 \end{bmatrix}. \tag{8}$$

Assume that the right-hand side of Eq. (4) is the inhomogeneous term of the equation. Then, the solution of Eq. (4), together with the boundary condition shown in Eq. (5), is expressed by the following volume integral equation:

$$u_i(x) = f_i(x, x_{(s)}) - \int_{\mathbb{R}^3_+} G_{ij}(x, y)N_{jk}(\partial_1, \partial_2, \partial_3, y)u_k(y)dy, \tag{9}$$

where f_i is the incident wave field and G_{ij} is the Green's function, which satisfies the following equations:

$$\begin{aligned} &(L_{ij}(\partial_1, \partial_2, \partial_3) + \delta_{ij}\rho_0\omega^2)G_{jk}(x, y) = -\delta_{ik}\delta(x - y), \\ &P^{(0)}_{ij}(\partial_1, \partial_2, \partial_3)G_{jk}(x, y) = 0, \quad (\text{at } x_3 = 0). \end{aligned} \tag{10}$$

Note that the components of $P^{(0)}_{ij}$ in Eq. (10) are as follows:

$$\left[P^{(0)}_{ij}(\partial_1, \partial_2, \partial_3)\right] = \begin{bmatrix} \mu_0\partial_3 & 0 & \mu_0\partial_1 \\ 0 & \mu_0\partial_3 & \mu_0\partial_2 \\ \lambda_0\partial_1 & \lambda_0\partial_2 & (\lambda_0 + 2\mu_0)\partial_3 \end{bmatrix}. \tag{11}$$

By means of the Green's function, the incident wave field is expressed as:

$$f_i(x, x_{(s)}) = G_{ij}(x, x_{(s)})q_j, \tag{12}$$

It is convenient to express the volume integral equation in terms of the scattered wave field:

$$v_i(x) = u_i(x) - f_i(x, x_{(s)}), \tag{13}$$

which becomes as follows:

$$\begin{aligned} v_i(x) = &-\int_{\mathbb{R}^3_+} G_{ij}(x, y)N_{jk}(\partial_1, \partial_2, \partial_3, y)f_k(y, x_{(s)})dy \\ &- \int_{\mathbb{R}^3_+} G_{ij}(x, y)N_{jk}(\partial_1, \partial_2, \partial_3, y)v_k(y)dy. \end{aligned} \tag{14}$$

In the derivation of the volume integral equation shown in Eq. (9) based on Eqs. (4) and (5), the radiation condition of the wave field was assumed. However, like the Sommerfeld radiation condition (Sommerfeld, 1949), the explicit form of the radiation condition of the elastic wave field for the half space is very difficult to obtain. This is due to the presence of the Rayleigh wave and the body waves in an elastic half space. Therefore, instead of presenting the explicit form of the radiation condition for an elastic half space, we use the following formula:

$$\lim_{R\to\infty} \int_{S_R} \left(G_{ij}(x, y)\tau_j(y) - T_{ij}(x, y)u_j(y)\right)dS_R = 0 \quad x \in \mathbb{R}^3_+, y \in S_R, \tag{15}$$

as the radiation condition, where S_R is the surface of the semisphere defined by

$$S_R = \left\{x \in \mathbb{R}^3_+ | x_1^2 + x_2^2 + x_3^2 = R^2\right\}, \tag{16}$$

τ_j is the traction vector, and T_{ij} is the double layer kernel of the Green's function.

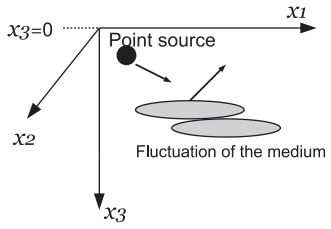

Fig. 1. Concept of the analyzed model.

2.2. Generalized Fourier transform for the volume integral equation

The generalized Fourier transform and inverse transform for elastic wave propagation in a half space (Touhei, 2009) have an important role in solving Eq. (14). These transforms are given as follows (Touhei, 2009):

$$(\mathcal{U}_{ij}u_j)(\xi) = \int_{\mathbb{R}^3_+} \Lambda^*_{ji}(\xi,x)u_j(x)dx, \tag{17}$$

$$\left(\mathcal{U}_{ij}^{-1}\hat{u}_j\right)(x) = \int_{\mathbb{R}^2} \sum_{\xi\in\sigma_p} \Lambda_{ij}(\xi,x)\hat{u}_j(\xi)d\xi_1 d\xi_2 + \int_{\mathbb{R}^2}\int_{\xi_r}^{+\infty} \Lambda_{ij}(\xi,x)\hat{u}_j(\xi)d\xi_3 d\xi_1 d\xi_2, \tag{18}$$

for $u_j \in L_2(\mathbb{R}^3_+)$ and $\hat{u}_j \in L_2(\sigma_p)\oplus L_2(\sigma_c)$, where $\xi=(\xi_1,\xi_2,\xi_3)\in\mathbb{R}^3_+$ is the point in the wavenumber space:

$$\xi_r = \sqrt{\xi_1^2+\xi_2^2}. \tag{19}$$

In addition, Λ_{ij} is the kernel of the generalized Fourier transform obtained from the following eigenvalue problem:

$$\begin{aligned} &L_{ij}(\partial_1,\partial_2,\partial_3)\Lambda_{jk}(\xi,x) = -\mu_0\xi_3^2\Lambda_{ik}(\xi,x),\\ &P^{(0)}_{ij}(\partial_1,\partial_2,\partial_3)\Lambda_{jk}(\xi,x) = 0, \quad (\text{at } x_3=0), \end{aligned} \tag{20}$$

where the superscript $*$ for Λ_{ij} denotes the complex conjugate and σ_p and σ_c are the subsets of the wavenumber space used to express the Rayleigh wave and the body waves, respectively, which are given as:

$$\begin{aligned} &\sigma_p = \left\{\xi=(\xi_1,\xi_2,\xi_3)\in\mathbb{R}^3_+ | F(\xi_r,\xi_3)=0\right\},\\ &\sigma_c = \left\{\xi=(\xi_1,\xi_2,\xi_3)\in\mathbb{R}^3_+ | \xi_3>\xi_r\right\}. \end{aligned} \tag{21}$$

Note that $F(\xi_r, \xi_3)$ in Eq. (21) is the Rayleigh function (Aki and Richards, 1980) expressed as:

$$F(\xi_r,\xi_3) = \left(2\xi_r^2-\xi_3^2\right)^2 - 4\xi_r^2\nu\gamma, \tag{22}$$

where ν and γ in Eq. (22) are denoted by

$$\nu^2 = \xi_r^2-\xi_3^2, \quad \gamma^2 = \xi_r^2-\xi_3^2(c_T/c_L)^2. \tag{23}$$

The kernel of the generalized Fourier transform has the following orthogonality relation:

$$\int_{\mathbb{R}^3_+} \Lambda^*_{ij}(\xi',x)\Lambda_{ik}(\xi,x)dx = \delta_{jk}\delta_{\xi_3,\xi_3'}\delta(\xi_1-\xi_1')\delta(\xi_2-\xi_2'), \tag{24}$$

when ξ, $\xi'\in\sigma_p$ and

$$\int_{\mathbb{R}^3_+} \Lambda^*_{ij}(\xi',x)\Lambda_{ik}(\xi,x)dx = \delta_{jk}\delta(\xi_1-\xi_1')\delta(\xi_2-\xi_2')\delta(\xi_3-\xi_3'), \tag{25}$$

when ξ, $\xi'\in\sigma_c$, where $\delta_{\xi_3,\xi_3'}$ is defined as:

$$\delta_{\xi_3,\xi_3'} = \begin{cases} 1 & (\text{when } \xi_3=\xi_3'),\\ 0 & (\text{when } \xi_3\neq\xi_3'), \end{cases} \tag{26}$$

The generalized Fourier transform and the inverse Fourier transform have the following structures, which clarify the algorithm for their transforms:

$$\hat{u}_i(\xi) = (\mathcal{U}_{ij}u_j)(\xi) = \left(\mathcal{F}^{(v)}_{im}\ T^*_{jm}\ \mathcal{F}^{(h)}u_j\right)(\xi), \tag{27}$$

$$u_i(x) = (\mathcal{U}_{ij}^{-1}\hat{u}_j)(x) = \left(\mathcal{F}^{(h)^{-1}}\ T_{im}\ \mathcal{F}^{(v)^{-1}}_{mj}\ \hat{u}_j\right)(x), \tag{28}$$

where $\mathcal{F}^{(h)}$ and $\mathcal{F}^{(h)^{-1}}$ are the ordinary Fourier integral transforms with respect to the horizontal coordinates defined by

$$\begin{aligned} \left(\mathcal{F}^{(h)}u\right)(\xi_1,\xi_2,x_3) &= \frac{1}{2\pi}\int_{\mathbb{R}^2} u(x)\exp(-i\xi_1x_1-i\xi_2x_2)dx_1dx_2,\\ \left(\mathcal{F}^{(h)^{-1}}\bar{u}\right)(x_1,x_2,x_3) &= \frac{1}{2\pi}\int_{\mathbb{R}^2} \bar{u}(\xi_1,\xi_2,x_3)\exp(i\xi_1x_1+i\xi_2x_2)d\xi_1d\xi_2. \end{aligned} \tag{29}$$

In addition, T_{ij} is the unitary matrix, the components of which are:

$$[T_{ij}] = \begin{bmatrix} 0 & i\xi_1/\xi_r & i\xi_2/\xi_r\\ 0 & i\xi_2/\xi_r & -i\xi_1/\xi_r\\ 1 & 0 & 0 \end{bmatrix}, \tag{30}$$

and $\mathcal{F}^{(v)}_{im}$ and $\mathcal{F}^{(v)^{-1}}_{mj}$ are the transforms with respect to the vertical coordinate defined by

$$\left(\mathcal{F}^{(v)}_{mj}\bar{u}_j\right)(\xi) = \int_0^\infty \psi_{jm}(\xi,x_3)\bar{u}_j(\xi_1,\xi_2,x_3)dx_3, \tag{31}$$

$$\left(\mathcal{F}^{(v)^{-1}}_{im}\hat{u}_m\right)(\xi_1,\xi_2,x_3) = \sum_{\xi\in\sigma_p}\psi_{im}(\xi,x_3)\hat{u}_m(\xi) + \int_{\xi_r}^\infty \psi_{im}(\xi,x_3)\hat{u}_m(\xi)d\xi_3. \tag{32}$$

Note that the overbar of u indicates that $\bar{u}$ is a function having (ξ_1, ξ_2, x_3) as arguments.

The kernel of the transform with respect to the vertical coordinate system $\psi_{ij}(\xi, x_3)$ is the solution of the equation of the eigenvalue problem:

$$\widehat{L}_{ij}\psi_{jk}(\xi,x_3) = \mu_0\xi_3^2\psi_{ik}(\xi,x_3), \tag{33}$$

with the free boundary condition:

$$\widehat{P}^{(0)}_{ij}\psi_{jk}(\xi,x_3) = 0, \quad (\text{at } x_3=0), \tag{34}$$

where $\widehat{L}_{ij}$ and $\widehat{P}_{ij}$ are the operators obtained from:

$$\begin{aligned} \widehat{L}_{ij} &= -T^*_{mi}L_{mk}(i\xi_1,i\xi_2,\partial_3)T_{kj},\\ \widehat{P}^{(0)}_{ij} &= T^*_{mi}P^{(0)}_{mk}(i\xi_1,i\xi_2,\partial_3)T_{kj}, \end{aligned} \tag{35}$$

the components of which are:

$$\widehat{L}_{ij} = \begin{bmatrix} -(\lambda_0+2\mu_0)\partial_3^2+\mu_0\xi_r^2 & (\lambda_0+\mu_0)\xi_r\partial_3 & 0\\ -(\lambda_0+\mu_0)\xi_r\partial_3 & -\mu_0\partial_3^2+(\lambda_0+2\mu_0)\xi_r^2 & 0\\ 0 & 0 & -\mu_0\partial_3^2+\mu_0\xi_r^2 \end{bmatrix}, \tag{36}$$

$$\widehat{P}^{(0)}_{ij} = \begin{bmatrix} (\lambda_0+2\mu_0)\partial_3 & -\lambda_0\xi_r & 0\\ \mu_0\xi_r & \mu_0\partial_3 & 0\\ 0 & 0 & \mu_0\partial_3. \end{bmatrix}. \tag{37}$$

The explicit forms of ψ_{ij} are summarized in the next section. These explicit forms are important in order to formulate and clarify the fast method for the volume integral equation.

The Green's function for an elastic half space can be expressed by the kernel of the generalized Fourier transform. Application of the generalized Fourier transform to Eq. (10) yields the following equation:

$$\left(\mu_0\xi_3^2-\rho_0\omega^2\right)\widehat{G}_{kj}(\xi,y) = \Lambda^*_{jk}(\xi,y), \tag{38}$$

where $\widehat{G}_{kj}$ is the generalized Fourier transform of the Green's function. Based on Eq. (38), the Green's function can be expressed in the following form:

$$G_{ij}(x,y) = \int_{\mathbb{R}^2}\sum_{\xi\in\sigma_p}\frac{\Lambda_{ik}(\xi,x)\Lambda^*_{jk}(\xi,y)}{\mu_0\xi_3^2-\rho_0\omega^2+i\epsilon}d\xi_1d\xi_2 + \int_{\mathbb{R}^2}\int_{\xi_r}^\infty \frac{\Lambda_{ik}(\xi,x)\Lambda^*_{jk}(\xi,y)}{\mu_0\xi_3^2-\rho_0\omega^2+i\epsilon}d\xi_3d\xi_1d\xi_2, \tag{39}$$

where ϵ is an infinitesimally small positive number and the right-hand side is the limit as ϵ approaches zero. The term ϵ indicates how to avoid a singular point in the integrand (Aki and Richards, 1980). In the numerical calculation stage, a small positive finite real number must be imposed on ϵ in order to stabilize the numerical solutions.

Next, let us apply the generalized Fourier transform to Eq. (14). The volume integral equation is modified as follows:

$$\hat{v}_i(\xi) = -\hat{h}(\xi)\mathcal{U}_{ik}N_{kj}f_j - \hat{h}(\xi)\mathcal{U}_{ik}N_{kj}\mathcal{U}_{jl}^{-1}\hat{v}_l(\xi), \quad \left(\xi \in \sigma_p \cup \sigma_c \subset \mathbb{R}^3_+\right), \quad (40)$$

where $\hat{h}(\xi)$ is the function defined by

$$\hat{h}(\xi) = \frac{1}{\mu_0\xi_3^2 - \rho_0\omega^2 + i\epsilon}. \quad (41)$$

Eq. (40) can be regarded as the Fredholm equation as expressed in the following form:

$$\hat{v}_i(\xi) = \hat{b}_i(\xi) - \mathcal{A}_{ij}\hat{v}_j(\xi), \quad \left(\xi \in \sigma_p \cup \sigma_c \subset \mathbb{R}^3_+\right), \quad (42)$$

where $\hat{b}_i$ and $\mathcal{A}_{ij}$ are defined by

$$\hat{b}_i(\xi) = -\hat{h}(\xi)\mathcal{U}_{ik}N_{kj}f_j, \quad (43)$$

and

$$\mathcal{A}_{ij} = \hat{h}(\xi)\mathcal{U}_{ik}N_{kl}\mathcal{U}_{lj}^{-1}, \quad (44)$$

Eq. (42) is discretized, and the Krylov subspace is constructed for the operator to formulate a method for the volume integral equation. In this article, the Bi-CGSTAB method (Barrett et al., 1994) is used for the Krylov subspace iteration method. The discretization of the operator is not performed by deriving a coefficient matrix. Instead, the discretized generalized Fourier transform and the inverse Fourier transform are directly used to express the effects of the operator. As a result, a method for obtaining the volume integral equation that does not require a coefficient matrix is realized.

At this point, the treatment of the derivatives using the generalized Fourier transform should be considered. Using Eq. (28), we find:

$$\partial_k u_i(x) = \mathcal{F}^{(h)^{-1}}(i\xi_k)\ T_{im}\ \mathcal{F}^{(v)^{-1}}_{mj}\hat{u}_j(\xi), \quad (45)$$

when $k = 1, 2$ and

$$\partial_3 u_i(x) = \mathcal{F}^{(h)^{-1}}\ T_{im}\ \partial_3\mathcal{F}^{(v)^{-1}}_{mj}\hat{u}_j(\xi), \quad (46)$$

where, according to Eq. (32):

$$\partial_3\mathcal{F}^{(v)^{-1}}_{mj}\hat{u}_j(\xi) = \sum_{\xi\in\sigma_p}\partial_3\psi_{im}(\xi,x_3)\hat{u}_m(\xi) + \int_{\xi_r}^{\infty}\partial_3\psi_{im}(\xi,x_3)\hat{u}_m(\xi)d\xi_3. \quad (47)$$

Therefore, it is not necessary to carry out the numerical differentiation in order to evaluate $N_{kj}\mathcal{U}_{jl}^{-1}\hat{v}_l(\xi)$ in Eq. (40). This also holds for the case in which Eq. (40) is used in a discretized form.

The CPU time required for the proposed method strongly depends on the algorithm for the generalized Fourier transform. Previously, however, a large amount of CPU time was found to be required for the generalized Fourier transform and the inverse Fourier transform (Touhei, 2009). The reason for this is the use of the trapezoidal approach for the integrals shown in Eqs. (31) and (32). Furthermore, the use of the trapezoidal approach causes a difficulty in obtaining accurate solutions for the case in which the parameter x_3 becomes large in Eq. (32). The reason for this is that $\Delta\xi_3$ for discretizing the integral of Eq. (32) must be set sufficiently small for a large x_3. This is clear from the explicit forms of the eigenfunctions presented in the next section. Therefore, unless we adjust the interval of grid points in the wavenumber domain according to the quantity of x_3, there is a limitation in the trapezoidal approach. A method by which to resolve the problems associated with the development of a fast and accurate algorithm for the generalized Fourier transform is discussed in the next section.

2.3. Fast method for solving the volume integral equation

Instead of the trapezoidal formula for Eqs. (31) and (32), we must seek an alternative method. This requires investigation of the explicit forms of ψ_{ij} as solutions of Eqs. (33) and (34).

2.3.1. Explicit forms of the solution to the eigenvalue problem (33) and (34)

The explicit forms of the solutions of Eqs. (33) and (34) are presented here for each case of $\xi \in \sigma_p$ and $\xi \in \sigma_c$, which are defined by Eq. (21). For the sake of convenience in presenting the solutions, σ_c is divided into two subsets:

$$\sigma_c = \sigma_{c1} \cup \sigma_{c2}, \quad (48)$$

where:

$$\begin{aligned}\sigma_{c1} &= \left\{\xi = (\xi_1,\xi_2,\xi_3) \in \mathbb{R}^3_+ | \xi_r < \xi_3 < (c_L/c_T)\xi_r\right\},\\ \sigma_{c2} &= \left\{\xi = (\xi_1,\xi_2,\xi_3) \in \mathbb{R}^3_+ | (c_L/c_T)\xi_r < \xi_3\right\}.\end{aligned} \quad (49)$$

The following coefficients Δ_j, $(j = 1,\cdots,8)$ attached to the solutions ψ_{ij} are used to satisfy the free boundary conditions as well as the normalization conditions. Note that, with the exception of the explicit forms listed below, ψ_{ij} are assumed to be zero. For the case in which $\xi \in \sigma_p$, the explicit forms of ψ_{ij} are expressed as:

$$\begin{aligned}\psi_{11}(\xi,x_3) &= -\gamma\exp(-\gamma x_3)\Delta_1 + \xi_r^2\exp(-\nu x_3)\Delta_2,\\ \psi_{21}(\xi,x_3) &= \xi_r\exp(-\gamma x_3)\Delta_1 - \xi_r\nu\exp(-\nu x_3)\Delta_2,\end{aligned} \quad (50)$$

where the coefficients Δ_1 and Δ_2 satisfy the following:

$$\Delta_1/\Delta_2 = \frac{2\xi_r^2\nu}{\nu^2+\xi_r^2}, \quad (51)$$

$$\frac{\gamma^2+\xi_r^2}{2\gamma}\Delta_1^2 - 2\xi_r^2\Delta_1\Delta_2 + \frac{\xi_r^2\left(\xi_r^2+\nu^2\right)}{2\nu}\Delta_2^2 = 1. \quad (52)$$

For the case in which $\xi \in \sigma_{c1}$, ψ_{ij} are given by

$$\begin{aligned}\psi_{11}(\xi,x_3) &= -\gamma\exp(-\gamma x_3)\Delta_3 + \xi_r^2\cos(\bar{\nu}x_3)\Delta_4 + \xi_r^2\sin(\bar{\nu}x_3)\Delta_5,\\ \psi_{21}(\xi,x_3) &= \xi_r\exp(-\gamma x_3)\Delta_3 - \xi_r\bar{\nu}\sin(\bar{\nu}x_3)\Delta_4 + \xi_r\bar{\nu}\cos(\bar{\nu}x_3)\Delta_5,\\ \psi_{33}(\xi,x_3) &= \xi_r\cos(\bar{\nu}x_3)\Delta_6,\end{aligned} \quad (53)$$

where $\bar{\nu} = \sqrt{\xi_3^2-\xi_r^2}$ and the coefficients Δ_j, $(j = 3,\ldots,6)$ must satisfy the following:

$$\begin{aligned}\Delta_4 &= \alpha(\xi)\Delta_3,\\ \Delta_5 &= \beta(\xi)\Delta_3,\\ \Delta_4^2+\Delta_5^2 &= \frac{2}{\pi}\frac{1}{\bar{\nu}\xi_r^2\xi_3},\\ \Delta_6 &= \frac{1}{\xi_r}\sqrt{\frac{2\xi_3}{\pi\bar{\nu}}}.\end{aligned} \quad (54)$$

In Eq. (54), α and β are defined by

$$\alpha(\xi) = \frac{2\gamma}{\xi_r^2-\bar{\nu}^2}, \quad \beta(\xi) = \frac{\bar{\nu}^2-\xi_r^2}{2\xi_r^2\bar{\nu}}, \quad (55)$$

For the case in which $\xi \in \sigma_{c2}$, ψ_{ij} are given as

$$\begin{aligned}
\psi_{11}(\xi,x_3) &= [\bar{\gamma}\cos(\bar{\gamma}x_3) + \bar{\alpha}(\xi)\xi_r^2\cos(\bar{\nu}x_3)]\Delta_7,\\
\psi_{21}(\xi,x_3) &= [\xi_r\sin(\bar{\gamma}x_3) - \bar{\alpha}(\xi)\xi_r\bar{\nu}\sin(\bar{\nu}x_3)]\Delta_7,\\
\psi_{12}(\xi,x_3) &= [-\bar{\gamma}\sin(\bar{\gamma}x_3) + \beta(\xi)\xi_r^2\sin(\bar{\nu}x_3)]\Delta_8,\\
\psi_{22}(\xi,x_3) &= [\xi_r\cos(\bar{\gamma}x_3) + \beta(\xi)\xi_r\bar{\nu}\cos(\bar{\nu}x_3)]\Delta_8,\\
\psi_{33}(\xi,x_3) &= \xi_r\cos(\bar{\nu}x_3)\Delta_6,
\end{aligned} \tag{56}$$

where $\bar{\gamma} = \sqrt{(c_T/c_L)^2\xi_3^2 - \xi_r^2}$ and the coefficients Δ_7 and Δ_8 are:

$$\begin{aligned}
\Delta_7^2 &= \frac{\pi}{2}\frac{1}{\xi_3(\bar{\gamma} + \bar{\alpha}^2\xi_r^2\bar{\nu})},\\
\Delta_8^2 &= \frac{\pi}{2}\frac{1}{\xi_3(\bar{\gamma} + \beta^2\xi_r^2\bar{\nu})},
\end{aligned} \tag{57}$$

where

$$\bar{\alpha}(\xi) = \frac{2\bar{\gamma}}{\bar{\nu}^2 - \xi_r^2}. \tag{58}$$

2.3.2. Decomposition of the operator $\mathcal{F}^{(v)}$

Based on the explicit forms of ψ_{ij}, we modify Eqs. (31) and (32). The basic concept for this modification is the decomposition of an equation into the ordinary Laplace and Fourier sine and cosine transforms. In this situation, we must replace the parameters of the integrals ξ_3 with γ, ν, $\bar{\nu}$, and $\bar{\gamma}$ for the inverse transform. Furthermore, the modification of Eqs. (31) and (32) should also be expressed in comprehensive form, even if explicit forms of ψ_{ij} are complicated. Considering these facts, let the modification of Eqs. (31) and (32) be expressed as:

$$\begin{aligned}
\mathcal{F}_{ij}^{(v)}\bar{u}_j &= A_{ij}^{L\gamma}\mathcal{L}_\gamma[\bar{u}_j] + A_{ij}^{Lv}\mathcal{L}_v[\bar{u}_j] + A_{ij}^{Fc\bar{\gamma}}\mathcal{F}_{c\bar{\gamma}}[\bar{u}_j] + A_{ij}^{Fs\bar{\gamma}}\mathcal{F}_{s\bar{\gamma}}[\bar{u}_j]\\
&\quad + A_{ij}^{Fc\bar{\nu}}\mathcal{F}_{c\bar{\nu}}[\bar{u}_j] + A_{ij}^{Fs\bar{\nu}}\mathcal{F}_{s\bar{\nu}}[\bar{u}_j],\\
\mathcal{F}_{ij}^{(v)^{-1}}\hat{u}_j &= \mathcal{L}_{\gamma(p)}^*\left[A_{ij}^{L^*\gamma(p)}\hat{u}_j\right] + \mathcal{L}_{v(p)}^*\left[A_{ij}^{L^*v(p)}\hat{u}_j\right]\\
&\quad + \mathcal{L}_\gamma^*\left[A_{ij}^{L^*\gamma}\hat{u}_j\right] + \mathcal{F}_{c\bar{\gamma}}^*\left[A_{ij}^{F^*c\bar{\gamma}}\hat{u}_j\right] + \mathcal{F}_{s\bar{\gamma}}^*\left[A_{ij}^{F^*s\bar{\gamma}}\hat{u}_j\right]\\
&\quad + \mathcal{F}_{c\bar{\nu}}^*\left[A_{ij}^{F^*c\bar{\nu}}\hat{u}_j\right] + \mathcal{F}_{s\bar{\nu}}^*\left[A_{ij}^{F^*s\bar{\nu}}\hat{u}_j\right],
\end{aligned} \tag{59}$$

where $\mathcal{L}$, $\mathcal{F}_s$, and $\mathcal{F}_c$ are the operators for the Laplace and Fourier sine and cosine transforms, the subscripts γ, ν, $\bar{\gamma}$, and $\bar{\nu}$ of which denote the parameters for the transforms. In addition, the script $*$ for these operators indicates that the integrals are obtained by means of the parameters described by the subscripts, and (p) denotes the operator for the region of $\xi \in \sigma_p$. Here, $\mathcal{L}_\gamma$, $\mathcal{L}_v$, $\mathcal{L}_\gamma^*$, $\mathcal{L}_{\gamma(p)}^*$, $\mathcal{L}_{v(p)}^*$ $\mathcal{F}_{s\bar{\nu}}$, $\mathcal{F}_{s\bar{\nu}}^*$, $\mathcal{F}_{s\bar{\gamma}}$, and $\mathcal{F}_{s\bar{\gamma}}^*$ are the operators of the Laplace and Fourier sine transforms defined by

$$\begin{aligned}
\mathcal{L}_\Gamma[\bar{u}] &= \int_0^\infty \bar{u}(\xi_1,\xi_2,x_3)\exp(-\Gamma x_3)dx_3,\\
\mathcal{L}_\Gamma^*[\hat{u}] &= \int_0^\infty \hat{u}(\xi_1,\xi_2,\xi_3)\exp(-\Gamma x_3)d\Gamma,\\
\mathcal{L}_{\Gamma(p)}^*[\hat{u}] &= \sum_{\xi\in\sigma_p}\hat{u}(\xi_1,\xi_2,\xi_3)\exp(-\Gamma x_3),\\
\mathcal{F}_{s\bar{\Gamma}}[\bar{u}] &= \int_0^\infty \bar{u}(\xi_1,\xi_2,x_3)\sin(\bar{\Gamma}x_3)dx_3,\\
\mathcal{F}_{s\bar{\Gamma}}^*[\hat{u}] &= \int_0^\infty \hat{u}(\xi_1,\xi_2,\xi_3)\sin(\bar{\Gamma}x_3)d\bar{\Gamma},
\end{aligned} \tag{60}$$

where index Γ takes the value of γ or v. Here, $\mathcal{F}_{c\bar{\nu}}$, $\mathcal{F}_{c\bar{\nu}}^*$, $\mathcal{F}_{c\bar{\gamma}}$, and $\mathcal{F}_{c\bar{\gamma}}^*$ are the operators of the Fourier cosine transforms. The explicit forms of these operators are clear from Eq. (60). In addition, A_{ij}, e.g., $A_{ij}^{L^*\gamma(p)}$ and $A_{ij}^{L^*v(p)}$, in Eq. (59) are functions of the wavenumber that are clarified by the explicit forms of the eigenfunctions. For example:

$$A_{11}^{L^*\gamma(p)} = -\gamma\Delta_1, \quad A_{11}^{L^*v(p)} = \xi_r^2\Delta_2 \tag{61}$$

Note that the coefficients Δ_1 and Δ_2 can be determined by giving the wavenumber $\xi \in \sigma_p$. All other functions in Eq. (59) are given in the Appendix A.

2.3.3. Fast algorithm of the generalized Fourier transform

At this point, let us introduce the grid point model for an elastic half space shown in Fig. 2. In the figure, the concept of the block division for the grid point model is also added for the discussion of the MPI parallel processing provided later herein. The number of grid points of the model shown in Fig. 2 are $N_1 \times N_2 \times N_3$, where $N_1 \times N_2$ is the number of horizontal grid points and N_3 is the number of vertical grid points. Define D_X and D_Ξ as the sets of grid points for the space and wavenumber domains in the following form:

$$\begin{aligned}
D_X &= \{(n_1\Delta x_1, n_2\Delta x_2, n_3\Delta x_3)|n_1\in\mathbb{N}_1, n_2\in\mathbb{N}_2, n_3\in\mathbb{N}_3)\},\\
D_\Xi &= \{(n_1\Delta\xi_1, n_2\Delta\xi_2, \eta_R)|n_1\in\mathbb{N}_1, n_2\in\mathbb{N}_2, F(\xi_r,\eta_R) = 0\},\\
&\quad \oplus\left\{\left(n_1\Delta\xi_1, n_2\Delta\xi_2, \sqrt{n_3^2\Delta\bar{\nu}^2 + \xi_r^2}\right)|n_1\in\mathbb{N}_1, n_2\in\mathbb{N}_2, n_3\in\mathbb{N}_3)\right\}
\end{aligned} \tag{62}$$

where $\mathbb{N}_1$, $\mathbb{N}_2$, and $\mathbb{N}_3$ are the sets of integers given as:

$$\begin{aligned}
\mathbb{N}_1 &= \{n| -N_1/2 \leqslant n < N_1/2\},\\
\mathbb{N}_2 &= \{n| -N_2/2 \leqslant n < N_2/2\},\\
\mathbb{N}_3 &= \{n|0 \leqslant n < N_3\}.
\end{aligned} \tag{63}$$

Δx_j, $(j = 1,2,3)$ are the intervals of the grid in the space domain. $\Delta\xi_j$, $(j = 1,2)$ are the horizontal intervals of the grid in the wavenumber domain, and $\Delta\bar{\nu}$ is the interval for discretizing $\mathcal{F}_{s\bar{\nu}}^*$ and $\mathcal{F}_{c\bar{\nu}}^*$, which are included in the operator $\mathcal{F}_{ij}^{(v)^{-1}}$. Recall the structure of the generalized Fourier transform shown in Eqs. (27) and (28). We use these structures in the following discretized forms:

$$\begin{aligned}
\hat{u}_i(\xi) &= \left(\mathcal{F}_{(D)im}^{(v)}T_{(D)mj}^*\mathcal{F}_{(D)}^{(h)}u_j\right)(\xi), \quad (\xi\in D_\Xi),\\
u_i(x) &= \left(\mathcal{F}_{(D)}^{(h)-1}T_{(D)mi}^*\mathcal{F}_{(D)mj}^{(v)-1}\hat{u}_j\right)(x), \quad (x\in D_X),
\end{aligned} \tag{64}$$

where the subscript (D) denotes that the operator is in discretized form. For example, $\mathcal{F}_{(D)}^{(h)}$ and $\mathcal{F}_{(D)}^{(h)-1}$ are expressed as:

$$\begin{aligned}
\left(\mathcal{F}_D^{(h)}[u]\right)(\bar{x}^{(l,n)}) &= \frac{\Delta x_1\Delta x_2}{2\pi}\sum_{k\in\mathbb{N}_1\times\mathbb{N}_2}u(x^{(k,n)})\exp\left(-ix^{(k,n)}\cdot\bar{x}^{(l,n)}\right),\\
\left(\mathcal{F}_D^{(h)^{-1}}[\bar{u}]\right)(x^{(k,n)}) &= \frac{\Delta\xi_1\Delta\xi_2}{2\pi}\sum_{l\in\mathbb{N}_1\times\mathbb{N}_2}\bar{u}(\bar{x}^{(l,n)})\exp\left(ix^{(k,n)}\cdot\bar{x}^{(l,n)}\right),
\end{aligned} \tag{65}$$

where

$$k = (k_1,k_2)\in\mathbb{N}_1\times\mathbb{N}_2, \quad l = (l_1,l_2)\in\mathbb{N}_1\times\mathbb{N}_2, \tag{66}$$

$$x^{(k,n)} = (k_1\Delta x_1, k_2\Delta x_2, n\Delta x_3), \quad \bar{x}^{(l,n)} = (l_1\Delta\xi_1, l_2\Delta\xi_2, n\Delta x_3), \quad (n\in\mathbb{N}_3), \tag{67}$$

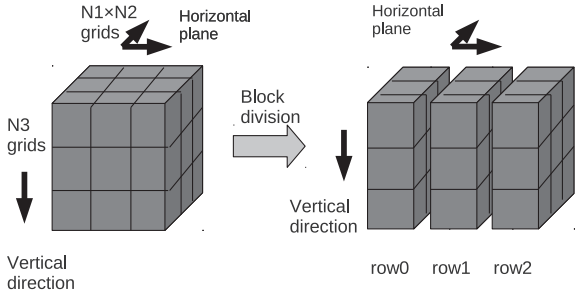

Fig. 2. Grid point model of the ground and the bock division of the model.

and

$$x^{(k,n)} \cdot \bar{x}^{(l,n)} = k_1 l_1 \Delta x_1 \Delta \xi_1 + k_2 l_2 \Delta x_2 \Delta \xi_2. \tag{68}$$

The discretized forms of $\mathcal{F}_{ij}^{(v)}$ and $\mathcal{F}_{ij}^{(v)-1}$ are very complicated. However, it is possible to present the elements of these operators that constitute $\mathcal{F}_{ij}^{(v)}$ and $\mathcal{F}_{ij}^{(v)-1}$. For example, $\mathcal{F}_{(D)s\bar{v}}$, $\mathcal{F}^*_{(D)s\bar{v}}$, $\mathcal{F}_{(D)c\bar{v}}$, and $\mathcal{F}^*_{(D)c\bar{v}}$ are:

$$\begin{aligned}
\left(\mathcal{F}_{(D)s\bar{v}}[\bar{u}]\right)\left(\xi^{(l,m)}\right) &= \Delta x_3 \sum_{n=0}^{N_3-1} \bar{u}\left(\bar{x}^{(l,n)}\right) \sin\left(x_3^{(n)}\bar{v}^{(m)}\right),\\
\left(\mathcal{F}^*_{(D)s\bar{v}}[\hat{u}]\right)\left(\bar{x}^{(l,n)}\right) &= \Delta \bar{v} \sum_{m=0}^{N_3-1} \hat{u}\left(\xi_3^{(l,m)}\right) \sin\left(x_3^{(n)}\bar{v}^{(m)}\right),\\
\left(\mathcal{F}_{(D)c\bar{v}}[\bar{u}]\right)\left(\xi^{(l,m)}\right) &= \Delta x_3 \sum_{n=0}^{N_3-1} \bar{u}\left(\bar{x}^{(l,n)}\right) \cos\left(x_3^{(n)}\bar{v}^{(m)}\right),\\
\left(\mathcal{F}^*_{(D)c\bar{v}}[\hat{u}]\right)\left(\bar{x}^{(l,n)}\right) &= \Delta \bar{v} \sum_{m=0}^{N_3-1} \hat{u}\left(\xi^{(l,n)}\right) \cos\left(x_3^{(n)}\bar{v}^{(m)}\right),
\end{aligned} \tag{69}$$

where

$$x_3^{(n)} = n\Delta x_3, \quad \bar{v}^{(m)} = m\Delta\bar{v}, \tag{70}$$

and

$$\xi^{(l,m)} = \left(l_1\Delta\xi_1, l_2\Delta\xi_2, \sqrt{\xi_r^2 + m^2\Delta\bar{v}^2}\right). \tag{71}$$

Likewise, the discretized forms of the Laplace transforms are:

$$\left(\mathcal{L}_{(D)\gamma}[\bar{u}]\right)\left(\xi^{(l,m)}\right) = \Delta x_3 \sum_{n=0}^{N_3-1} \bar{u}\left(\bar{x}^{(l,n)}\right) \exp\left(-\gamma^{(m)}x_3^{(n)}\right), \tag{72}$$

$$\left(\mathcal{L}_{(D)v}[\bar{u}]\right)\left(\xi^{(l,l_p)}\right) = \Delta x_3 \sum_{n=0}^{N_3-1} \bar{u}\left(\bar{x}^{(l,n)}\right) \exp\left(-v^{(l_p)}x_3^{(n)}\right), \tag{73}$$

$$\left(\mathcal{L}^*_{(D)\gamma}[\hat{u}]\right)\left(\bar{x}^{(l,n)}\right) = \Delta\bar{v} \sum_{m=0}^{M} \hat{u}\left(\xi^{(l,m)}\right) \exp\left(-\gamma^{(m)}x_3^{(n)}\right), \tag{74}$$

$$\gamma^{(m)} = \sqrt{\xi_r^2 - (c_T/c_L)^2\left(\xi_r^2 + m^2\Delta\bar{v}^2\right)}, \tag{75}$$

and M is the maximum value of m that satisfies:

$$\xi_r^2 - (c_T/c_L)^2\left(\xi_r^2 + m^2\Delta\bar{v}^2\right) \geqslant 0. \tag{76}$$

The arguments $v^{(l_p)}$ and $\xi^{(l,l_p)}$ in Eq. (73) are expressed by

$$v^{(l_p)} = \sqrt{\xi_r^2 - \xi_3^2}, \quad \xi^{(l,l_p)} = (l_1\Delta\xi_1, l_2\Delta\xi_2, \xi_3), \tag{77}$$

where ξ_3 satisfies $F(\xi_r, \xi_3) = 0$.

The relationship of the interval of the grid points between the space and wavenumber domains is as follows:

$$\begin{aligned}
\Delta x_i \Delta\xi_i &= \frac{2\pi}{N_i}, \quad (i = 1, 2),\\
\Delta x_3 \Delta\bar{v} &= \frac{\pi}{N_3}.
\end{aligned} \tag{78}$$

As can be seen in Eq. (78), the interval of grid points in the space and the wavenumber domain restrict each other according to the structures of the Fourier transform and the Fourier sine and cosine transforms. This point differs from the trapezoidal approach, the numerical results of which will be presented later herein.

It is also necessary to obtain $\Delta\bar{\gamma}$ in order to discretize the operators $\mathcal{F}^*_{c\bar{\gamma}}$ and $\mathcal{F}^*_{s\bar{\gamma}}$. In the present study, the parameter $\Delta\bar{\gamma}$ is set to be equal to $\Delta\bar{v}$. The use of the interval $\Delta\bar{\gamma}$, however, requires points in the wavenumber domain that are not in D_Ξ, even if $\Delta\bar{v} = \Delta\bar{\gamma}$. The set of the grid points in the wavenumber domain required by the use of $\Delta\bar{\gamma}$ is:

$$\begin{aligned}
D'_\Xi = \{&(n_1\Delta\xi_1, n_2\Delta\xi_2, \eta_R) | n_1 \in \mathbb{N}_1, n_2 \in \mathbb{N}_2, F(\xi_r, \eta_R) = 0\}\\
&\oplus \left\{ \left(n_1\Delta\xi_1, n_2\Delta\xi_2, (c_L/c_T)\sqrt{n_3^2\Delta\bar{\gamma}^2 + \xi_r^2}\right)\right.\\
&\left. | n_1 \in \mathbb{N}_1, n_2 \in \mathbb{N}_2, n_3 \in \mathbb{N}_3 \right\}.
\end{aligned} \tag{79}$$

A linear interpolation scheme is introduced in the present study in order to adjust the gap of the grid intervals caused by the presence of $\Delta\bar{v}$ and $\Delta\bar{\gamma}$. Namely, the results of the grid interval due to operators $\mathcal{F}_{c\bar{\gamma}}$ and $\mathcal{F}_{s\bar{\gamma}}$ are adjusted and embedded into D_Ξ.

It is evident that fast algorithms are applicable to all of the operators for the Fourier transforms. The fast algorithm is also applicable to the Laplace transform. In the present study, the fast algorithm for the Laplace transform developed by Strain (1992) is used. The algorithm for the discrete generalized Fourier transforms is shown in Fig. 3. The algorithm described in Fig. 3 is based on the structure of the transform shown in Eq. (64). For Fig. 3, the function $u_j(ip, kk)$ defined at the grid points in the space domain is transformed into the functions $\hat{u}^{(R)}(ip)$ and $\hat{u}_j^{(B)}(ip, kk)$ defined at the grid points in the wavenumber domain, where ip, ($ip = 1, \ldots, N_1N_2$) is the parameter defining the horizontal components of the grid points, kk, ($kk = 1, \ldots, N_3$) is the parameter defining the vertical components of the grid points, $\hat{u}^{(R)}(ip)$ is the function for the Rayleigh wave, and $\hat{u}_j(ip, kk)$ is the function for the body wave components. According to Eq. (64), the first task of the generalized Fourier transform is the application of $\mathcal{F}_{(D)}^{(h)}$ and the second task is the multiplication of $T^*_{(D)mj}$. The application of $\mathcal{F}_{(D)}^{(h)}$, which is expressed as FFT2D in Fig. 3, must be repeated N_3 times and that of $T^*_{(D)mj}$ must be repeated $N_1 \times N_2 \times N_3$ times. The final task for the transform $\mathcal{F}_{ij}^{(v)}$, which is expressed as FFTV1D in Fig. 3, must be repeated $N_1 \times N_2$ times. The amount of computation for FFT2D is $O(N_1N_2\log(N_1N_2))$ and that of FFT1DV is $O(N_3\log N_3)$ due to the 1D fast Fourier transform. Note that the amount of computation for the fast Laplace transform included in FFT1DV is $O(N_3)$, which is smaller than that of the fast Fourier transform. As a result, the amount of computation of the generalized Fourier transform is found to be $O(N\log N)$, where $N = N_1N_2N_3$, which is the number of grid points for the elastic half space. The amount of computation for the fast generalized Fourier transform will be verified later through numerical examples.

```
do  kk = 1, ··· , N3
      do  ip = 1, ··· , N1 * N2
            w_j(ip) ← u_j(ip, kk),      (j = 1, 2, 3)
      end do
       apply FFT2D to w_j → y_j,  (j = 1, 2, 3)
      do  ip = 1, ··· , N1 * N2
            ū_i(ip, kk) ← T*_ji y_j(ip),   (i, j = 1, 2, 3)
      end do
end do

do  ip = 1, ··· , N1 * N2
      do  kk = 1, ··· , N3
            w_j(kk) ← ū_j(ip, kk),    (j = 1, 2, 3)
      end do
       apply FFT1DV to w_j → z^(R) and z_j^(B),   (j = 1, 2, 3)
       z^(R) → û^(R)(ip)
      do  kk = 1, ··· , N3
       z_j^(B)(kk) → û_j^(B)(ip, kk),    (j = 1, 2, 3)
      end do
end do
```

Fig. 3. Fast algorithm of the discretized form of the generalized Fourier transform. Note that w_m, y_m, $\bar{u}_j$, $z^{(R)}$, and $z_j^{(B)}$ are the temporary work areas.

```
do  kk = 1, ··· , N3
      do  ip = ista, ··· , iend
            wj(ip) ← uj(ip, kk),      (j = 1, 2, 3)
      end do
      apply mpi allgatherv to wj,  (j = 1, 2, 3)
       apply FFT2D to wj → yj,  (j = 1, 2, 3)
      do  ip = ista, ··· , iend
            ūi(ip, kk) ← T*ji yj,   (j = 1, 2, 3)
      end do
end do

do  ip = ista, ··· , iend
      do  kk = 1, ··· , N3
            wj(kk) ← ūj(ip, kk),    (j = 1, 2, 3)
      end do
       apply FFT1DV to wj → z(R) and z(B)j ,   (j = 1, 2, 3)
       z(R) → û(R)(ip)
      do  kk = 1, ··· , N3
       z(B)j (kk) → û(B)j (ip, kk),    (j = 1, 2, 3)
      end do
end do
```

Fig. 4. Parallel algorithm of the discretized form of the generalized Fourier transform. Note that w_m, y_m, $\bar{u}_j$, $z^{(R)}$, and $z_j^{(B)}$ are the temporary work areas.

Table 1
Properties of the material used for the background structure.

λ_0 (GPa)	μ_0 (GPa)	ρ_0 (g/cm^3)
4.0	2.0	2.0

A reduction in CPU time is expected by the introduction of the MPI parallel algorithm (Pacheco, 1997). According to Fig. 3, the longest loop is that for the parameter *ip*, which is related to the number of horizontal grid points. Let us apply the block division to the *ip* loop. The concept of this block division for the grid points model is exemplified in Fig. 2, in which three rows are used for the division. As shown in Fig. 2, the grid points model is divided in the vertical direction. The physical quantities defined at the grid points are stored separately in a memory of each row by means of dynamic allocation. The algorithms using block division are shown in Fig. 4, where the *ip* loop is from (ista) to (iend) instead of from 1 to $N_1{*}N_2$. Since the block division is in the vertical direction, MPI communication is required before calling FFT2D. Except for the MPI communication before FFT2D, the calculation of the generalized Fourier transforms can be carried out separately in each row. The efficiency of the parallel algorithms is discussed in the next section.

At the end of the formulation of the proposed method, the advantages and disadvantages of the present method, as compared with the boundary integral equation method, should be mentioned here. The advantage of the present method is that it is possible to treat a fluctuating inhomogeneous wave field, to which the boundary integral equation method is not easily applicable. Furthermore, the fluctuation is not necessarily smooth or closed. In a previous study (Touhei et al., 2009), two types of fluctuation models were used for numerical calculations. One model was bounded but discontinuous, and the other model was expressed in the form of the rapid decrease function (Reed and Simon, 1980). Despite these advantages, the uniform interval of the grid points required in the proposed method may restrict the accurate modeling of the geometry of the scattering object. This requirement is a disadvan-

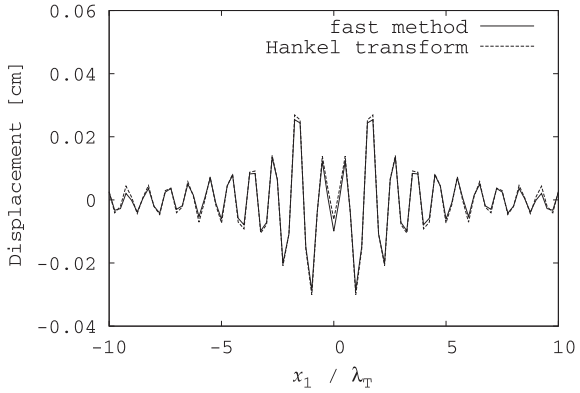

(a) Comparison of the fast generalized Fourier transform with the Hankel transform

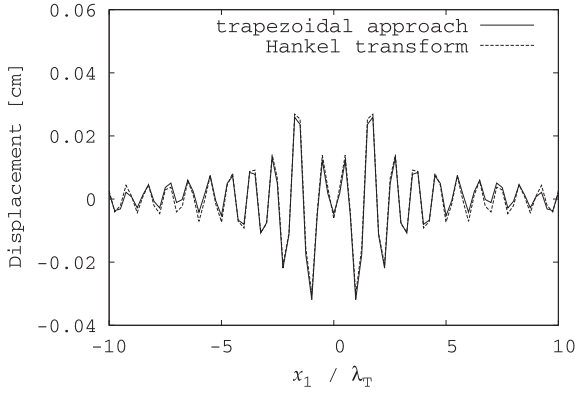

(b) Comparison of the trapezoidal approach with the Hankel transform

Fig. 5. Comparison of the Green's function at the free surface.

tage of the proposed method. In contrast, the boundary integral equation method does not suffer from this problem.

3. Numerical examples

3.1. Green's function composed by the generalized Fourier transform

First, for numerical examples, let us check the accuracy of the fast generalized Fourier transform by composing the Green's function. For the numerical calculations, the background Lamé constants and mass density of an elastic half space are summarized in Table 1, from which the P and S wave velocities are found to be 2 and 1 km/s, respectively, and that of the Rayleigh wave becomes approximately 0.93 km/s. In order to synthesize the Green's function, the direction of the excitation force is set in the vertical direction. The amplitude and excitation frequency of the force are 1×10^7 kN and 1.0 Hz, respectively. In addition, the location of the point force is at a depth of 1 km from the surface of the origin of the horizontal coordinate. For the fast generalized transform, D_X and D_Ξ shown in Eq. (62) are set such that $N_1 = N_2 = 256$, $N_3 = 128$, and $\Delta x_1 = \Delta x_2 = \Delta x_3 = 0.25$ km. As a result, $\Delta\xi_1$, $\Delta\xi_2$, and $\Delta\bar{\nu}$ become:

$$\Delta\xi_j = \frac{2\pi}{N_j \Delta x_j} = 0.09817\ \mathrm{km}^{-1}, \quad (j = 1, 2), \tag{80}$$

$$\Delta\bar{\nu} = \frac{\pi}{N_3 \Delta x_3} = 0.09817\ \mathrm{km}^{-1}. \tag{81}$$

The results of the Green's function composed by the trapezoidal approach are also examined here. For the trapezoidal approach, $N_j = 256$, $\Delta x_j = 0.25$ km, and $\Delta\xi_j = 0.09817\ \mathrm{km}^{-1}$, $(j = 1,2,3)$ are used. In addition, ϵ for $\hat{h}(\xi)$ shown in Eq. (41) is set at 0.60 for both the fast method and the trapezoidal approach. The background constants for the wave field, the number of grid points defined above, the amplitude and the direction of the point source, and the excitation frequency will also be used in the numerical examples presented hereinafter.

Fig. 5 compares the Green's functions at the free surface along the x_1 axis calculated by the fast generalized Fourier transform, the trapezoidal approach, and the Hankel transform. Note that the x_1 axis in Fig. 5 is expressed dimensionless form as x_1/λ_T, where λ_T is the wavelength of the S wave. The displacements in the vertical direction are compared. These comparisons reveal that the results of these three methods agree well. The quantitative discrepancy among these results, which is calculated as follows:

$$\epsilon_D = \frac{\sqrt{\sum |X_i - Y_i|^2}}{\sqrt{\sum |Y_i|^2}}, \tag{82}$$

reveals that $\epsilon_D = 0.13$, where X_i is the result of the trapezoidal approach and Y_i is the result of the Hankel transform. In addition, $\epsilon_D = 0.10$ is obtained, when X_i is the result of the fast generalized Fourier transform and Y_i is the result of the Hankel transform. The discrepancy of the results between the Hankel transform and the fast generalized Fourier transform is smaller than that between the trapezoidal approach and the Hankel transform. The treatment of the Hankel transform is not complicated, as compared to the treatment of the generalized Fourier transform. Therefore, the discrepancy indicates that the results of the fast generalized Fourier transform are more accurate than those of the trapezoidal approach.

Fig. 6 shows the distribution of the displacement amplitudes of the Green's function in a vertical plane of $x_2 = 0$ km. These numerical results are characterized by the Rayleigh wave propagation along the free surface, the body wave propagation downward, and the high-amplitude area caused by the singularity of the point source. The results obtained by the Hankel transform and the fast generalized Fourier transform are similar. On the other hand, the results obtained by the trapezoidal approach reveal an unnatural vertical band below the source point. Furthermore, several rays, which cannot be observed in other cases, are caused by this unnatural vertical band. The trapezoidal approach has difficulty in composing the Green's function in the region that x_3 become large as pointed out earlier.

3.2. Effects of the number of sampling grid points on the scattering analysis

The following examples for the numerical calculations are used to examine the effects of the sampling of grid points on the scattering analysis. For the analysis, the location of the source point $x_{(s)}$ is given by

$$x_{(s)} = (5, 0, 1) \quad (\mathrm{km}). \tag{83}$$

In addition, the fluctuations of the wave field are set by

$$\tilde{\lambda}(x) = A_\lambda \exp\left(-\eta_\lambda |x - x_c|^2\right), \qquad \tilde{\mu}(x) = A_\mu \exp\left(-\eta_\mu |x - x_c|^2\right), \tag{84}$$

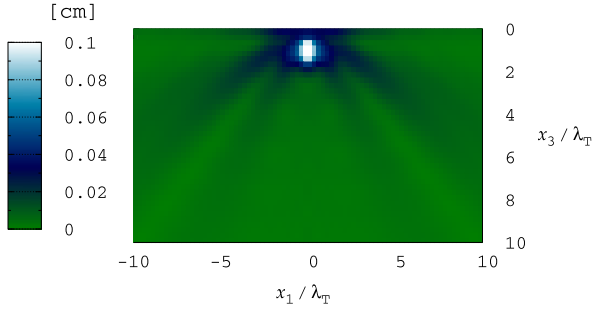

(a) Hankel transform

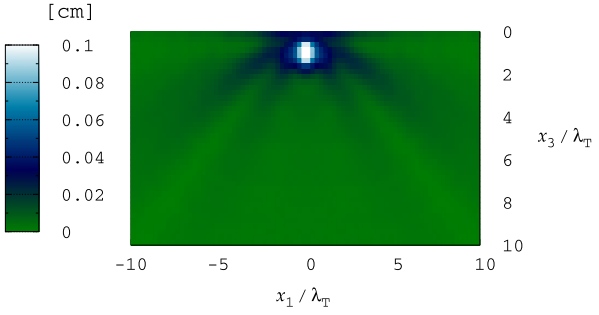

(b) Fast generalized Fourier transform

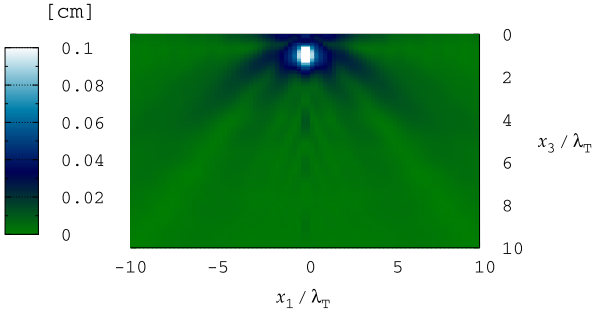

(c) Trapezoidal approach

Fig. 6. Comparison of the Green's function in a vertical plane.

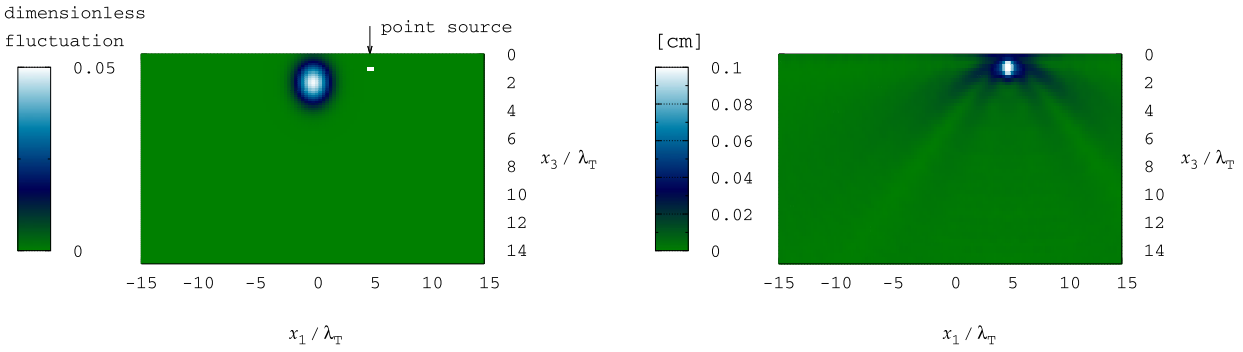

(a) Fluctuations of $\tilde{\lambda}$ and $\tilde{\mu}$ in the wave field (b) Incident wave field

Fig. 7. Fluctuations of the wave field and the incident wave field.

where x_c is the center of the fluctuating region, which is:

$$x_c = (0, 0, 2) \quad (\text{km}). \tag{85}$$

The parameters A_λ, A_μ, η_λ, and η_μ for Eq. (84) describe the amplitudes and spreads of the fluctuations, which are given as:

$$\begin{aligned} A_\lambda &= A_\mu = 0.2 \quad (\text{GPa}), \\ \eta_\lambda &= \eta_\mu = 0.5 \quad (\text{km}^{-2}). \end{aligned} \tag{86}$$

The fluctuation model, together with the incident wave field at the $x_2 = 0$ km plane, are shown in Fig. 7, which clarifies how the incident wave propagates toward the fluctuated area. Note that the fluctuation model in Fig. 7 is described in terms of the dimensionless Lamé constants $\tilde{\lambda}/\mu$ and $\tilde{\mu}/\mu$.

For the analysis by the fast method, eight cases are considered, whereas four cases are considered for the analysis by the trapezoidal approach. The sampling of grid points and the interval of the grid points in the space domain for each case are summarized in Tables 2 and 3. For all of the cases, ϵ for $\hat{h}(\xi)$ shown in Eq. (41) is set at 1.0, which is larger than that used to calculate the Green's function in the previous section. The reason for this is that it is necessary to eliminate numerical errors caused by the iterative process. Due to the limitation of the available computer memory, the maximum number of grid points for the trapezoidal approach is $256 \times 256 \times 512$, whereas that for the fast method is $512 \times 512 \times 256$. The number of sampling grid points for the fast method is twice that for the trapezoidal approach because parallel computing by means of PC clusters is possible in the case of the fast method.

Table 2
Case studies for comparison of the interval and the number of grid points for scattering analysis by the fast method.

Case	N_1	N_2	N_3	Δx_1	Δx_2	Δx_3
case-F1	512	512	256	0.125	0.125	0.125
case-F2	512	512	256	0.25	0.25	0.25
case-F3	512	512	128	0.125	0.125	0.25
case-F4	256	256	128	0.125	0.125	0.125
case-F5	256	256	128	0.25	0.25	0.25
case-F6	256	256	64	0.25	0.25	0.25
case-F7	256	256	64	0.25	0.25	0.50
case-F8	128	128	64	0.25	0.25	0.25

Table 3
Case studies for comparison of the interval and the number of grid points for scattering analysis by the trapezoidal approach.

Case	N_1	N_2	N_3	Δx_1	Δx_2	Δx_3
case-T1	256	256	512	0.25	0.25	0.125
case-T2	256	256	512	0.25	0.25	0.25
case-T3	256	256	512	0.125	0.125	0.25
case-T4	256	256	256	0.25	0.25	0.25

Fig. 8 shows the results of the scattering analysis obtained by means of the fast method from case-F1 to case-F8. Fig. 8(a) and (b) show the results for case-F1 and case-F2, in which the number of sampling grid points is $512 \times 512 \times 256$. The difference between case-F1 and case-F2 is the grid intervals in the space domain, which are 0.125 and 0.25 km, respectively. According to the comparison of case-F1 and case-F2, significant differences cannot be seen. Fig. 8(c) shows the results of case-F3, the number of sampling grid points of which is $512 \times 512 \times 128$ and the intervals are $\Delta x_1 = \Delta x_2 = 0.125$ and $\Delta x_3 = 0.25$ km. Significant differences also cannot be seen in the result of case-F3 as compared to case-F1 and case-F2.

On the other hand, the scattered wave shown in Fig. 8(d) for case-F4 clearly differs from that in the previous three cases. Several unnatural high-amplitude bands can be observed from the bottom right to the top left of the figure. The sampling number and the interval of grid points for this case are $256 \times 256 \times 128$ and 0.125 km, respectively. Namely, the number of sampling grid points for this case is half that for case-F1, whereas the interval of the grid points is equal to case-F1. The problem observed in case-F4 is resolved in Fig. 8(e) for case-F5 by setting the interval of grid points in a space domain that is twice that of case-F4. Note that the interval of grid points in the wavenumber domain for case-F5 is equal to that of case-F1. Therefore, the interval of grid points in the wavenumber domain is more important than that in the space domain for the purpose of obtaining accurate solutions.

Fig. 8(f) and (g) show the results for case-F6 and case-F7, in which the number of sampling grid points is $256 \times 256 \times 64$, and the horizontal interval of grid points is 0.25 km. The difference between the models for these two cases is the vertical grid intervals, which are 0.25 and 0.5 km, respectively. Comparison of case-F6 and case-F7 revealed no significant differences other than that in the spread of the scattered waves around the fluctuated area. Due to the coarse vertical interval of grid points in the space domain for case-F7, the spread of the scattered waves is not clearer for case-F7, as compared to case-F6.

Fig. 8(h) shows the results for case-F8, in which several unnatural high-amplitude bands can be seen from the bottom right to the top left of the figure, as shown in Fig. 8(d). The sampling number and the interval of grid points for this case are $128 \times 128 \times 64$ and 0.25 km, respectively. Due to the reduction in the number of sampling grid points for case-F8 from case-F7, the interval of grid points in the wavenumber domain has increased. As a result, the problem of unnatural results occurred again.

Although the above case studies are limited, the problem of numerical calculation is found to be caused by the large interval

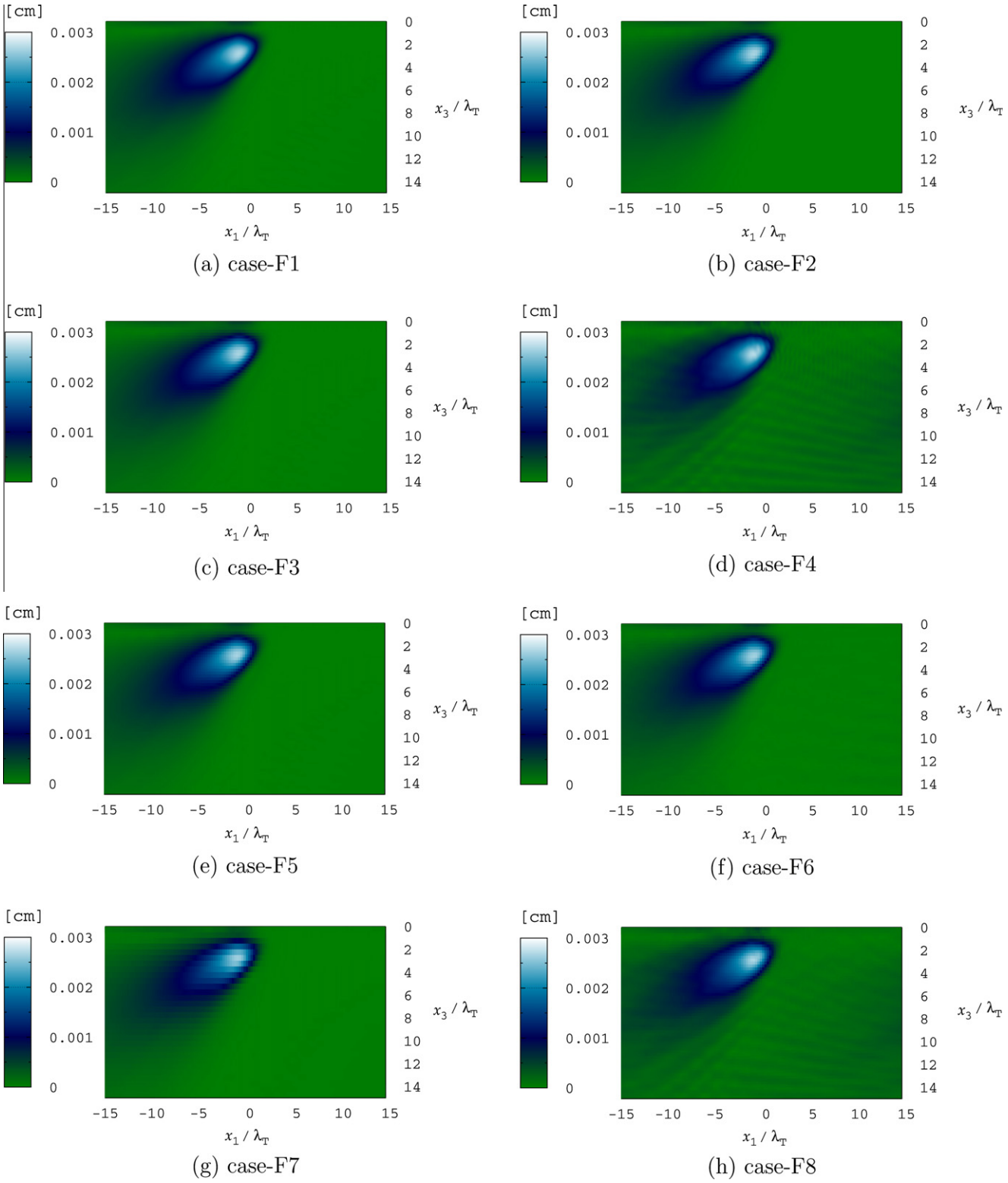

Fig. 8. Displacement amplitudes of the scattered waves obtained by the fast method.

of grid points in the wavenumber domain. The numerical calculations are always successful for the case in which:

$$\lambda_T \Delta\xi \leqslant 0.09817, \tag{87}$$

where $\Delta\xi$ represents the interval of grid points in the wavenumber domain. In this sense, the number of sampling grid points, i.e., $256 \times 256 \times 128$, is sufficient to obtain the converged solution for the case in which the spatial interval of grid points, $\Delta x_j = 0.25$ km, is used in the analysis.

As mentioned earlier in the formulation of the present method, the volume integral equation in the wavenumber domain is solved by the Bi-CGSTAB method. The results obtained here are obtained through only two iterations of the Bi-CGSTAB method based on the convergence properties of the solutions of the

volume integral equation. The convergence properties of the solutions with respect to the number of iterations will be discussed in the next section. The discussion at this stage considers the relationship between the number of sampling grid points and the CPU time required for the scattering analysis due to two iterations in the fast method.

Fig. 9 shows this relationship. The horizontal axis of Fig. 9 shows $N\log(N)$, where $N = N_1 \times N_2 \times N_3$. The CPU time obtained here is based on two-core parallel processing and two iterations. In Fig. 9, the observed CPU times are plotted, and the fitting line is applied to these plots. It is clear that the CPU times are approximately proportional to $N\log(N)$. Therefore, based on the numerical calculations, the amount of calculation proportional to $N\log(N)$ for the fast method is verified.

Fig. 10 shows the results of the scattering analysis obtained by the trapezoidal approach. The number of sampling grid points for case-T1 through case-T3 are $256 \times 256 \times 512$, and that for case-T4 is $256 \times 256 \times 256$. The grid interval of the wavenumber space for the trapezoidal approach is determined by the following formula:

$$\Delta\xi_j = \frac{2\pi}{N_j \Delta x_j}, \quad (j = 1, 2), \qquad \Delta\xi_3 = \frac{1}{2}\Delta\xi_1. \tag{88}$$

The Bi-CGSTAB method is used to obtain the solutions presented in the following. Two iterations were sufficient to converge the solutions, with the exception of case-T4.

Comparison of the results for case-T1 and case-T2 reveals no significant differences. The difference in the analyzed models for these two cases are in the grid interval in the x_3 direction. Therefore, the difference in the grid interval in the x_3 direction did not affect the numerical results for these cases. There are, however, significant differences between the results obtained by the fast method and those obtained by the trapezoidal approach, which are particularly noticeable deep underground. These differences are due to the problem associated with the trapezoidal approach, in which it becomes difficult to obtain accurate solutions for a large x_3.

Fig. 10(c) shows the results for case-T3. For this case, the horizontal grid interval of $\Delta x_1 = \Delta x_2 = 0.125$ km, which is half that for case-T1 and case-T2. In this figure, unnatural high amplitude areas can be observed deep underground. One reason for the unnatural areas is related to the limitation of the trapezoidal approach. However, the fine horizontal grid interval in the space domain is also a cause of the problem, as can be seen in Fig. 8(d) and (f).

Fig. 10(d) shows the results for case-T4. For this case, the number of sampling grid points for the vertical direction is $N_3 = 256$, which is the smallest case for the trapezoidal approach. The results are very different from those for other cases and failed to converge. This indicates that the number of sampling grid points for N_3 was insufficient for the analysis. The results of the scattering analysis obtained using the trapezoidal approach indicate that the

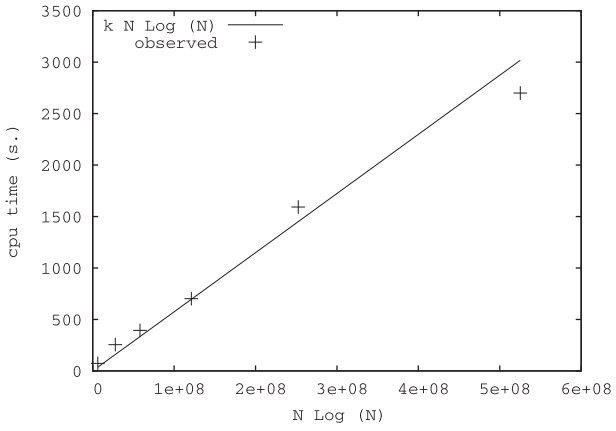

Fig. 9. Comparison of the CPU time with the number of grid points.

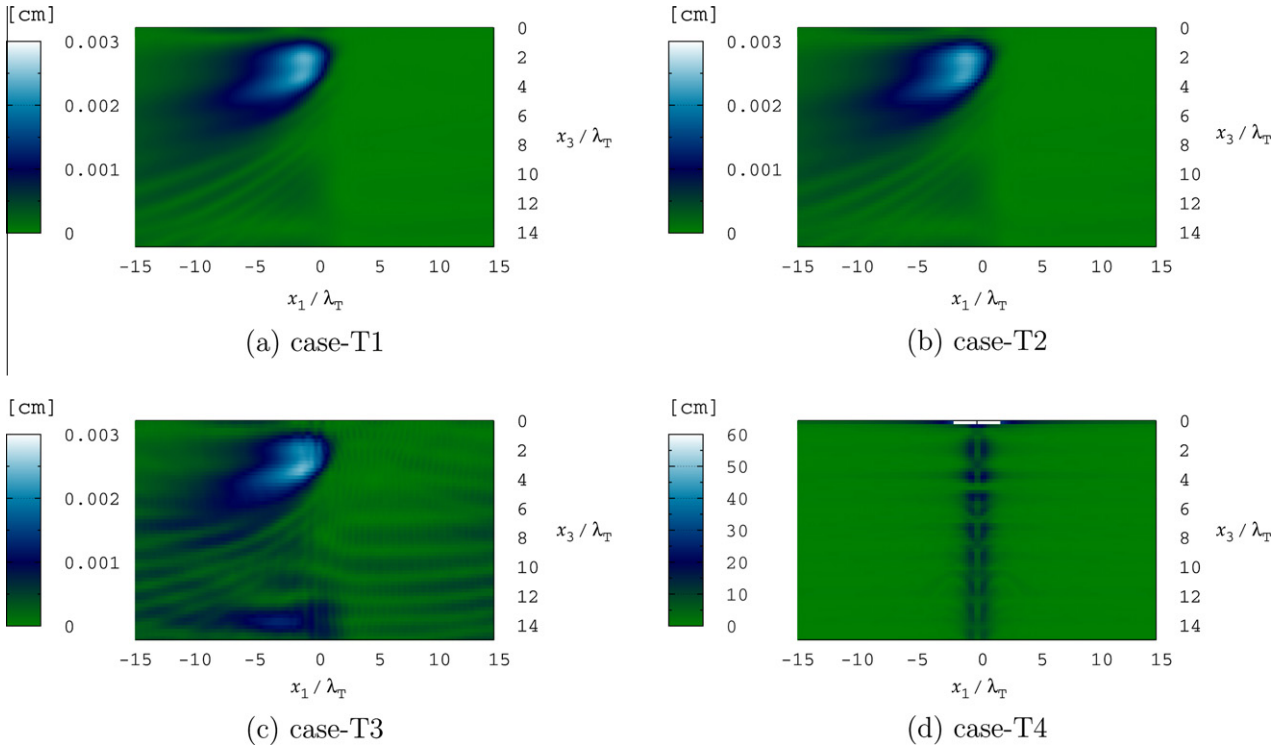

Fig. 10. Displacement amplitudes of the scattered waves due to the trapezoidal approach.

performance of this method in obtaining the wave field deep underground is poor. Furthermore, there was a case in which the solution failed to converge. On the other hand, the solution obtained by the fast method is found to be stable and solves the problem of the trapezoidal approach.

3.3. Convergence properties of the volume integral equation

Next, let us investigate the convergence properties of the volume integral equation. The relative error during the iterative process is defined by

$$\epsilon_r = \frac{\left\| \hat{v}_i + \mathcal{A}_{ij}\hat{v}_j - \hat{b}_i \right\|}{\left\| \hat{b}_i \right\|}, \tag{89}$$

according to Eq. (42), where $\|\cdot\|$ is the norm of the function in the wavenumber domain defined by

$$\|f_i(\xi)\|^2 = \sum_{\xi \in D_\Xi} \left[|f_1(\xi)|^2 + |f_2(\xi)|^2 + |f_3(\xi)|^2 \right]. \tag{90}$$

Fig. 11 shows the relationship between the relative error and the number of iterations, in which there is a rapid decrease in the relative error. The results shown in Fig. 8 were obtained after two iterations, where the relative error was found to be less than 1.0×10^{-3}.

Fig. 12 shows the effects of the number of iterations on the solutions of the volume integral equation. In Fig. 12, the solution is presented along the x_1 axis at the free surface. The proposed solution (results of two iterations) is compared with the solutions obtained by various numbers of iterations. Fig. 12(a) compares proposed solution and the Born approximation (no iterations). The differences in the displacement amplitude can be observed in the region just above the fluctuated area, where the displacement amplitude due to the Born approximation is larger than that due to the proposed method. In the region of forward scattering, the methods are in almost complete agreement. In the region of backward scattering, however, the phase and amplitude differ, and even the displacement amplitudes are very small. Fig. 12(b) shows a comparison of the proposed solution and the solution for one iteration. The figure reveals that the results are in almost complete agreement, which coincides the convergence properties of the solution shown in Fig. 11. The quantitative discrepancy of the Born

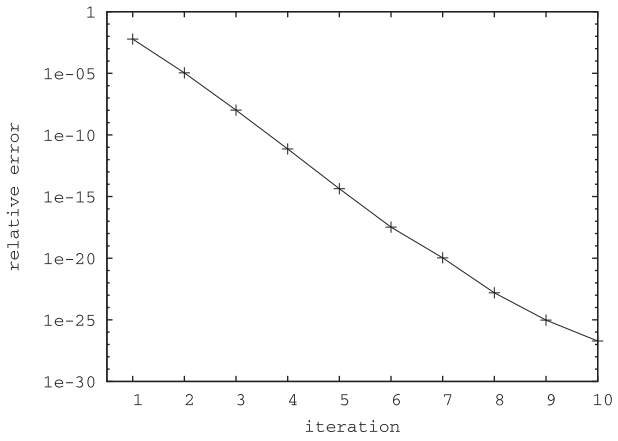

Fig. 11. Convergence of the solution by the Bi-CGSTAB method.

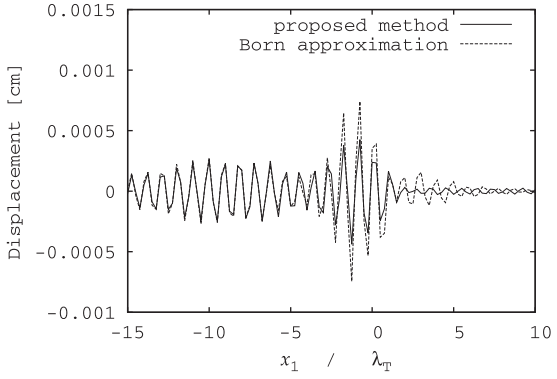

(a) Comparison of the proposed solution with the Born approximation

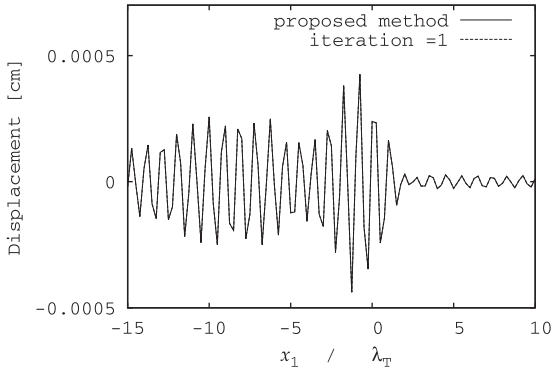

(b) Comparison of the proposed solution with the solution obtained by one iteration

Fig. 12. Effect of the number of iterations of scattered waves along the x_1 axis.

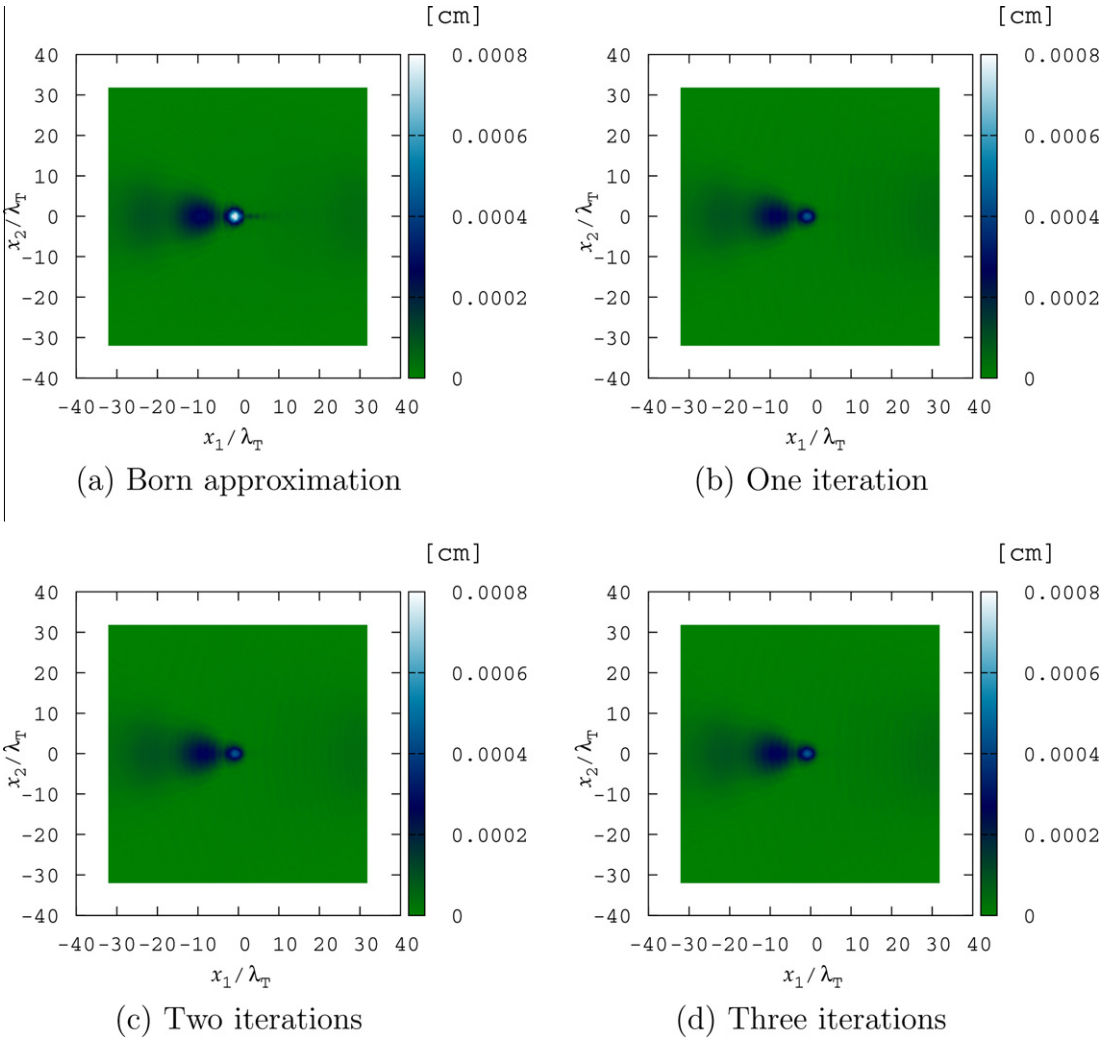

Fig. 13. Effect of the number of iterations on scattered waves at the free surface.

approximation from the proposed solution obtained from Eq. (82) is $\epsilon_D = 0.172$, where X_i is the result of the Born approximation and Y_i is the proposed solution. In addition, the discrepancies from the proposed solution are $\epsilon_D = 6.00 \times 10^{-3}$ and $\epsilon_D = 1.05 \times 10^{-5}$, for one and three iterations, respectively.

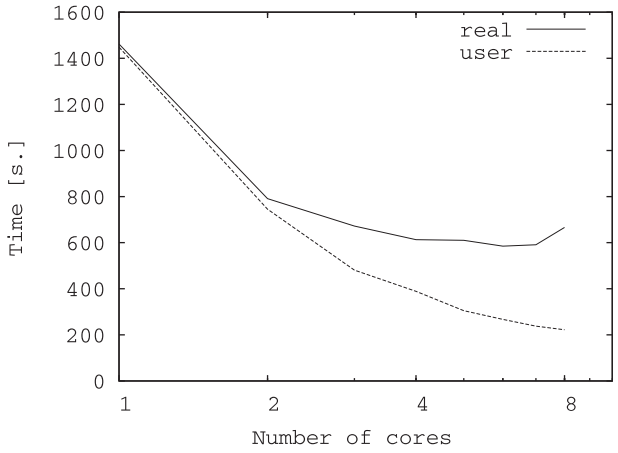

Fig. 14. Effect of the number of cores on parallel computation.

Fig. 13(a) through (d) show the distributions of displacement amplitudes at the free surface according to the number of iterations. The plots can be characterized by high-displacement-amplitude areas just above areas of fluctuation as well as a forward region. Fig. 13(a) shows the results of the Born approximation. The displacement amplitude of the region just above the area of fluctuation for this case is higher than other cases. In addition, the amplitude of the backward scattering can be also determined. Fig. 13(b) through (d) show the results obtained by one to three iterations, respectively. The patterns of the displacement amplitude for these three cases are similar. The convergence of the solution is found to be almost achieved by one iteration.

3.4. CPU time required for scattering analysis

Based on the numerical examples, the CPU time required for scattering analysis is discussed. The processor used for the computation was an AMD Opteron 2387 processor. For the parallel computation, it is necessary to investigate the relationship between the CPU time and the number of cores used for the computation. Fig. 14 clarifies its relationship for the case in which the $256 \times 256 \times 128$ grid point model was used. In Fig. 14, 'real' denotes the elapsed time and 'user' denotes the amount of CPU time spent in user-mode code. Fig. 14 indicates that the elapsed time decreases according to the increase in the number of cores. This de-

crease, however, has its limitations, and the use of more than four cores may not the best choice for the computation. On the other hand, the decrease in CPU time (expressed as 'user') is approximately proportional to the number of cores used. In the future, the possibility of reducing the gap between the 'real' time and the 'user' time must be examined.

As mentioned earlier, the solution of the volume integral equation obtained from the trapezoidal approach was not very accurate. In this sense, a strict discussion of the CPU time reduction generated by the trapezoidal approach to the fast method may not be meaningful. Even in this situation, the CPU time required by the trapezoidal approach based on the $256 \times 256 \times 512$ grid points model was 14 h and 18 min. On the other hand, the CPU time required by the proposed fast method was only 24 min for the case in which the $256 \times 256 \times 128$ grid point model was used for non-parallel processing. The number of iterations required in order to obtain the solution using the Bi-CGSTAB method was two for the both present method and the trapezoidal approach.

4. Conclusions

In the present paper, a fast method for the volume integral equation for elastic wave propagation in a half space was presented. The essential consideration in the formulation was related to the application of the fast generalized Fourier transform to the construction of the Krylov subspace. The fast transform was realized by decomposing the kernel of the transform into the ordinary Fourier and Laplace transforms. A method of MPI parallel computation for the proposed method was also presented.

Several numerical calculations were carried out in order to examine the effects of the interval and the number of sampling grid points on the numerical solutions. The numerical results and the structure of the generalized Fourier transform revealed that the amount of computations was $O(N\log N)$, where N is the number of grid points for the ground model. In addition, the coarse interval of grid points in the wavenumber domain was found to cause a problem in obtaining accurate solutions of the volume integral equation.

For the purpose of comparison, the trapezoidal approach for obtaining the volume integral equation was also examined. It was not easy to obtain accurate results deep underground using the trapezoidal approach. Furthermore, there was also a case in which the solution failed to converge using the trapezoidal approach. The fast method proposed herein resolved the problems associated with the trapezoidal approach. The fast method was also found to significantly reduce the CPU time.

Appendix A. Decomposition of the operators $\mathcal{F}^{(v)}$ and $\mathcal{F}^{(v)^{-1}}$

As demonstrated in the main text of the present paper, the generalized Fourier transform and the inverse Fourier transform for elastic wave propagation in a half space with respect to the vertical coordinate system are expressed as:

$$\begin{aligned}\mathcal{F}_{ij}^{(v)}\bar{u}_j &= A_{ij}^{L\gamma}\mathcal{L}_\gamma[\bar{u}_j] + A_{ij}^{Lv}\mathcal{L}_v[\bar{u}_j] + A_{ij}^{Fc\bar{\gamma}}\mathcal{F}_{c\bar{\gamma}}[\bar{u}_j] + A_{ij}^{Fs\bar{\gamma}}\mathcal{F}_{s\bar{\gamma}}[\bar{u}_j] \\ &\quad + A_{ij}^{Fc\bar{v}}\mathcal{F}_{c\bar{v}}[\bar{u}_j] + A_{ij}^{Fs\bar{v}}\mathcal{F}_{s\bar{v}}[\bar{u}_j], \\ \mathcal{F}_{ij}^{(v)^{-1}}\hat{u}_j &= \mathcal{L}_{\gamma(p)}^*\left[A_{ij}^{L*\gamma(p))}\hat{u}_j\right] + \mathcal{L}_{v(p)}^*\left[A_{ij}^{L*v(p))}\hat{u}_j\right] + \mathcal{L}_\gamma^*\left[A_{ij}^{L^*\gamma}\hat{u}_j\right] \\ &\quad + \mathcal{F}_{c\bar{\gamma}}^*\left[A_{ij}^{F^*c\bar{\gamma}}\hat{u}_j\right] + \mathcal{F}_{s\bar{\gamma}}^*\left[A_{ij}^{F^*s\bar{\gamma}}\hat{u}_j\right] + \mathcal{F}_{c\bar{v}}^*\left[A_{ij}^{F^*c\bar{v}}\hat{u}_j\right] + \mathcal{F}_{s\bar{v}}^*\left[A_{ij}^{F^*s\bar{v}}\hat{u}_j\right],\end{aligned} \tag{A.1}$$

where $\mathcal{L}_\gamma[\cdot]$, $\mathcal{L}_v[\cdot]$, $\mathcal{L}_\gamma^*[\cdot]$, $\mathcal{L}_{\gamma(p)}^*[\cdot]$, $\mathcal{L}_{v(p)}^*[\cdot]$, $\mathcal{F}_{s\bar{v}}$, $\mathcal{F}_{s\bar{v}}^*$, $\mathcal{F}_{s\bar{\gamma}}$, $\mathcal{F}_{s\bar{\gamma}}^*$, $\mathcal{F}_{c\bar{v}}$, $\mathcal{F}_{c\bar{v}}^*$, $\mathcal{F}_{c\bar{\gamma}}$, and $\mathcal{F}_{c\bar{\gamma}}^*$ denote the operators for the Laplace transform and the Fourier sine and cosine transforms given in the main text of the article in Eq. (60). The functions of the wavenumber $A_{ij}^{L\gamma}$, A_{ij}^{Lv}, $A_{ij}^{Fc\bar{\gamma}}$, $A_{ij}^{Fs\bar{\gamma}}$, $A_{ij}^{Fc\bar{v}}$, $A_{ij}^{Fs\bar{v}}$, $A_{ij}^{L*\gamma(p))}$, and $A_{ij}^{L*v(p))}$ are directly derived from the explicit forms of the eigenfunctions ψ_{ij} given in the main text of the article. For the case in which $\xi \in \sigma_p$, these functions are:

$$\begin{aligned}&A_{11}^{L*\gamma(p)} = -\gamma\Delta_1, \quad A_{11}^{L*v(p)} = \xi_r^2\Delta_2, \quad A_{21}^{L*\gamma(p)} = \xi_r\Delta_1, \\ &A_{21}^{L*v(p)} = -\xi_r v\Delta_2, \quad A_{11}^{L\gamma} = -\gamma\Delta_1, \quad A_{11}^{Lv} = \xi_r^2\Delta_2, \\ &A_{12}^{L\gamma} = \xi_r\Delta_1, \quad A_{12}^{Lv} = -\xi_r v\Delta_2.\end{aligned} \tag{A.2}$$

Next, for the case in which $\xi \in \sigma_p$, where $\xi_r < \xi_3 < (c_L/c_T)\xi_r$, these functions are given as:

$$\begin{aligned}&A_{11}^{L\gamma} = -\gamma\Delta_3, \quad A_{11}^{Fc\bar{v}} = \xi_r^2\Delta_4, \quad A_{11}^{Fs\bar{v}} = \xi_r\Delta_5, \quad A_{12}^{L\bar{\gamma}} = \xi_r\Delta_3, \\ &A_{12}^{Fs\bar{v}} = -\xi_r\bar{v}\Delta_4, \quad A_{12}^{Fc\bar{v}} = \xi_r\bar{v}\Delta_5, \quad A_{33}^{Fc\bar{v}} = \xi_r\Delta_6.\end{aligned} \tag{A.3}$$

In addition, for the case in which $\xi \in \sigma_p$, where $(c_L/c_T)\xi_r < \xi_3$, these functions are:

$$\begin{aligned}&A_{11}^{Fc\bar{\gamma}} = \gamma\Delta_7, \quad A_{11}^{Fc\bar{v}} = \bar{\alpha}(\xi)\xi_r^2\Delta_7, \quad A_{12}^{Fs\bar{\gamma}} = \xi_r\Delta_7, \\ &A_{12}^{Fs\bar{v}} = -\bar{\alpha}(\xi)\xi_r\bar{v}\Delta_7, \quad A_{21}^{Fs\bar{\gamma}} = -\gamma\Delta_8, \quad A_{21}^{Fs\bar{v}} = \beta(\xi)\xi_r^2\Delta_8, \\ &A_{22}^{Fc\bar{\gamma}} = \xi_r\Delta_8, \quad A_{22}^{Fc\bar{v}} = \beta(\xi)\xi_r\bar{v}\Delta_8, \quad A_{33}^{Fc\bar{v}} = \xi_r\Delta_6.\end{aligned} \tag{A.4}$$

The functions for the wavenumber $A_{ij}^{L^*\gamma}$, $A_{ij}^{F^*c\bar{\gamma}}$, $A_{ij}^{F^*s\bar{\gamma}}$, $A_{ij}^{F^*c\bar{v}}$, and $A_{ij}^{F^*s\bar{v}}$ are also obtained as follows for $(\xi_r < \xi_3 < \xi_r(c_L/c_T))$:

$$\begin{aligned}&A_{11}^{L^*\gamma} = -\frac{\gamma^2 c_L^2}{\xi_3 c_T^2}\Delta_3, \quad A_{11}^{F^*c\bar{v}} = \frac{\bar{v}\xi_r^2}{\xi_3}\Delta_4, \quad A_{11}^{F^*s\bar{v}} = \frac{\bar{v}\xi_r^2}{\xi_3}\Delta_5, \\ &A_{21}^{L^*\gamma} = \frac{\xi_r c_L^2}{\xi_3 c_T^2}\Delta_3, \quad A_{21}^{F^*s\bar{v}} = -\frac{\bar{v}^2\xi_r}{\xi_3}\Delta_4, \quad A_{21}^{F^*c\bar{v}} = \frac{\xi_r\bar{v}^2}{\xi_3}\Delta_5.\end{aligned} \tag{A.5}$$

For the region of $(c_L/c_T)\xi_r < \xi_3$:

$$\begin{aligned}&A_{11}^{F^*c\bar{\gamma}} = \frac{\bar{\gamma}^2 c_L^2}{\xi_3 c_T^2}\Delta_7, \quad A_{11}^{F^*c\bar{v}} = \frac{\bar{v}\bar{\alpha}\xi_r^2}{\xi_3}\Delta_7, \quad A_{21}^{F^*s\bar{\gamma}} = \frac{\bar{\gamma}\xi_r c_L^2}{\xi_3 c_T^2}\Delta_7, \\ &A_{21}^{F^*s\bar{v}} = -\frac{\bar{v}^2\xi_r\bar{\alpha}}{\xi_3}\Delta_7, \quad A_{12}^{F^*s\bar{\gamma}} = -\frac{\bar{\gamma}^2 c_L^2}{\xi_3 c_T^2}\Delta_8, \quad A_{21}^{F^*s\bar{v}} = \frac{\bar{v}\xi_r^2\beta}{\xi_3}\Delta_8, \\ &A_{22}^{F^*c\bar{\gamma}} = \frac{\xi_r\bar{\gamma}c_L^2}{\xi_3 c_T^2}\Delta_8, \quad A_{22}^{F^*c\bar{v}} = \frac{\beta\xi_r\bar{v}^2}{\xi_3}\Delta_8.\end{aligned} \tag{A.6}$$

$A_{33}^{F^*c\bar{v}}$ has the following form for the region $\xi \in \sigma_c$:

$$A_{33}^{F^*c\bar{v}} = \frac{\bar{v}\xi_r}{\xi_3}\Delta_6. \tag{A.7}$$

References

Aki, K., Richards, P.G., 1980. Quantitative Seismology, Theory and Methods. W.H. Freeman and Company.

Barrett, R., Berry, M., Chan, T.F., Demmel, J., Donato, J.M., Dongarra, J., Eijkhout, V., Pozo, R., Romine, C., Van der Vorst, H., 1994. Templates for the Solution of Linear Systems: Building Blocks for Iterative Methods. SIAM.

Colton, D., Kress, R., 1983. Integral Equation Methods in Scattering Theory. John Wiley and Sons Inc., New York.

Colton, D., Kress, R., 1998. Inverse Acoustic and Electromagnetic Scattering Theory. Springer, Berlin.

De Zaeytijd, J., Bogaert, I., Franchois, A., 2008. An efficient hybrid MLFMA-FFT solver for the volume integral equation in case of sparse 3D inhomogeneous dielectric scatterers. Journal of Computational Physics 227, 7052–7068.

Guzina, B.B., Fata, S.N., Bonnet, M., 2003. On the stress-wave imaging of cavities in a semi-infinite solid. International Journal of Solids and Structures 40, 1505–1523.

Hudson, J.A., Heritage, J.R., 1981. The use of the Born approximation in seismic scattering problems. Geophysical Journal Royal Astronomical Society 66, 221–240.

Ikebe, T., 1960. Eigenfunction expansion associated with the Schroedinger operators and their applications to scattering theory. Archive of Rational Mechanics and Analysis 5, 1–34.

Manolis, G.D., Dineva, P.S., Rangelov, T.V., 2004. Wave scattering by cracks in inhomogeneous continua using BIEM. International Journal of Solids and Structures 41, 3905–3927.

Pacheco, P.S., 1997. Parallel Programming with MPI. Morgan Kaufmann Publishers.

Reed, M., Simon, B., 1980. Methods of modern mathematical physics. Functional Analysis, vol. I. Academic Press.

Sommerfeld, A., 1949. Partial Differential Equations in Physics. Academic Press, New York.

Strain, J., 1992. A fast Laplace transform based on Laguerre functions. Mathematics of Computation 58, 275–283.
Touhei, T., 2003. Analysis of scattering waves in an elastic layered medium by means of the complete eigenfunction expansion form of the Green's function. International Journal of Solids and Structures 40, 3344–3377.
Touhei, T., 2009. Generalized Fourier transform and its application to the volume integral equation for elastic wave propagation in a half space. International Journal of Solids and Structures 46, 52–73.
Touhei, T., Kiuchi, T., Iwasaki, K., 2009. A fast volume integral equation method for the direct/inverse problem in elastic wave scattering phenomena. International Journal of Solids and Structures 46, 3860–3872.
Yang, J., Abubaker, A., van den Berg, P.M., Habashy, T.M., Reitich, F., 2008. A CG-FFT approach to the solution of a stress-velocity formulation of three-dimensional scattering problems. Journal of Computational Physics 227, 10018–10039.